Journal of Aerosol Science 193 (2026) 106758

Contents lists available at ScienceDirect

Journal of Aerosol Science

journal homepage: www.elsevier.com/locate/jaerosci

# The role of soot aggregate fusing in laminar flames: A study employing fusing models derived from carbon black

Daniel O'Sullivan, Stelios Rigopoulos *

*Department of Mechanical Engineering, Imperial College London, Exhibition Road, London, SW7 2AZ, UK*

ARTICLE INFO

Editor: Chris Hogan

*Keywords:*
Soot fusing
Soot aggregates
Carbonaceous particles
Laminar sooting flame
Population balance
CFD

ABSTRACT

The evolving morphology of carbonaceous aggregates has been previously ignored to a large extent in sooting flame studies. Soot aggregate fusing causes a reduction in surface area and the number of primary particles per aggregate. Despite soot aggregate fusing directly impacting the morphology of aggregates, there is no agreed model for the characteristic timescale for this process. Previous flame simulations used fusing timescale models based on other materials such as titania and silica, which feature different fusing mechanisms. Recently, a series of carbonaceous-based soot fusing models have been proposed that are intrinsically derived from carbonaceous materials such as carbon black or lab-produced ethylene soot. In the present work, these carbonaceous-material-based soot fusing models are implemented in a two population balance equation (PBE) framework and are further coupled with a reactive computational fluid dynamics (CFD) code in order to simulate the laminar Santoro series of flames across all three smoking conditions (non-smoking, incipient smoking, smoking). Predictions of soot volume fraction, total number density, number of primary particles per aggregate, and primary particle diameter are presented across all three flames and compared against experimental observations where possible. The importance of soot fusing is elucidated across various regions within flames and the predictive power of each fusing model is discussed.

## 1. Introduction

Carbonaceous aerosol nanoparticles such as soot, carbon black and synthesised nanomaterials appear in a wide range of environmental and engineering contexts. Environmental carbonaceous aerosols are second only to $CO_2$ in terms of climate forcing (Bond et al., 2013), while the health effects of inhaled soot particles range from respiratory damage to increased cancer risk (Niranjan & Thakur, 2017). On the other hand, synthesised carbonaceous particles have many uses; carbon black – with a global market of $18-20 bn (Emerton, 2024) – is used in tires, inks, batteries and solar cells, while new purpose-made carbonaceous nanoparticles include carbon quantum dots and carbon-coated nanoparticles for use as magnetic biofluids (Kelesidis et al., 2017).

Whether for mitigating environmental impacts or engineered synthesis, an understanding of the morphology of carbonaceous aerosols is essential. The aggregation of primary particles results in chain-like fractal structures and the inability to properly account for this morphology has been identified as one of the main sources of uncertainty in the prediction of optical properties of atmospheric particulates in global circulation models (Forestieri et al., 2018; Liu & Mishchenko, 2018). The surface area of fractal aggregates, which is greater than spherical particles, plays an important role in lung deposition (Vu et al., 2018) and in toxicity (Li et al., 2023; Tang et al., 2024). For engineered nanoparticles, control over morphology allows for the synthesis of tailored products for novel applications (Pratsinis, 2010).

* Corresponding author.
*E-mail address:* s.rigopoulos@imperial.ac.uk (S. Rigopoulos).

https://doi.org/10.1016/j.jaerosci.2026.106758
Received 17 September 2025; Received in revised form 28 January 2026; Accepted 29 January 2026
Available online 4 February 2026

The evolution of the morphology of particles in a reactive environment is complex and involves several physical and chemical processes, namely nucleation, surface growth and oxidation, aggregation and fusing. The combined effect of these processes can be studied with the aid of the population balance equation (PBE), which predicts the evolution of size and morphology distribution by linking it to the kinetics of the aforementioned processes (Rigopoulos, 2024). However, the process of fusing has received by far the least attention in studies of carbonaceous particles. This process refers to the gradual merging of the primary particles that make-up aggregates. Subsequently, the fusing process significantly modifies the structure and surface area of an aggregate. Despite its key role in dictating morphology, at present there is no established kinetic model for this process in the case of carbonaceous particles. Conversely, the sintering of inorganic particles such as silica has been extensively studied and established models exist.

The lack of attention given to fusing in soot literature can be attributed primarily to two reasons. Firstly, the underlying mechanisms driving fusing are not understood. Unlike inorganic nanoparticles, the fusing of carbonaceous particles can be due to a range of mechanisms — hence the use of the generic term 'fusing' (Michelsen et al., 2020). Therefore, simulations either do not include fusing kinetics or reuse models for the sintering of inorganic nanoparticles such as silica and titania. However, the underlying mechanisms are radically different in those materials: in silica it is a viscous flow mechanism while for titania it is transport by diffusion. The second reason is the inability of many PBE formulations used for sooting flame simulations to account for a fusing process with a finite timescale — see e.g. Raman and Fox (2016) and Rigopoulos (2019, 2024) for a review of them. This is because the inclusion of such a process requires accounting for aggregate morphology, which incurs an additional dimension to the population balance. A two-dimensional discretised PBE, such as the one proposed by Xiong and Pratsinis (1993) and Xiong et al. (1993) for the purpose of studying silica and titania nanoparticles, is too computationally expensive for implementation alongside computational fluid dynamics (CFD) simulations. A computationally feasible approach is to employ two coupled PBEs, one for the particle size distribution and one for a variable related to morphology such as the number of primary particles per aggregate. This formulation, which will be referred to as the two-PBE approach, involves discretisation of two one-dimensional equations rather than a one two-dimensional equation, and has been employed in two studies that included soot fusing (Sun et al., 2021; Veshkini et al., 2016). Another approach that does not suffer from the problem of dimensionality and has been used extensively for laminar flames, although it is too expensive for turbulent flames, is the Monte Carlo method. This approach has also been used in one study of laminar sooting flames that included soot fusing (Chen et al., 2013). However, in all of the aforementioned simulations, the fusing of soot was approached with models for the sintering of inorganic nanoparticles, in particular silica (Chen et al., 2013; Sun et al., 2021) and titania (Sun et al., 2021; Veshkini et al., 2016) and, as mentioned above, these materials feature radically different fusing mechanisms.

Recently, some authors have attempted to derive a model for soot fusing from data on carbonaceous material. Matsukawa et al. (2023) obtained a model from experimental data on ethylene- and benzene-derived soot in a pyrolitic reactor. O'Sullivan et al. (2025) recently derived two models for the fusing of carbonaceous nanoparticles via an inverse population balance methodology. In that work, a wide variety of soot and carbon black grades were examined, and a selection was chosen to be used as soot proxies. Subsequently, two models for the characteristic fusing timescale were derived using an inverse population balance that determined the most suitable form of the model on the basis of thermodynamic considerations, and the models were employed to simulate an inert reheating experiment (Ono et al., 2017). These works paved the way for the employment of soot fusing models derived from a carbonaceous material, but two important questions remain. First, none of the aforementioned models have been tested in the context of a flame simulation. Second, and perhaps more crucially, the impact of the fusing process in a sooting flame is still an open question due to the paucity of simulation studies that included fusing, all of which previously were with models extrapolated from inorganic materials.

The present paper aims to address these questions by simulating the well-known co-flow flame experiments performed by Santoro and co-workers (Santoro et al., 1983, 1987), one of the benchmark studies in the field of sooting flames. We concentrate on laminar flames in order to focus on the impact of fusing kinetics and the interplay of the various kinetic processes, without the additional complexity that turbulence brings to the problem. In essence, a laminar diffusion flame will exhibit all stages of the lifetime of soot, from formation, growth, and burnout (Santoro et al., 1983). Furthermore, distinct regions within the flame are associated with the dominance of various particulate processes. Our study concentrates on the two fusing models that were recently proposed by O'Sullivan et al. (2025), implemented in the context of a two-PBE approach in the form presented by Sun et al. (2021). In addition, the (Matsukawa et al., 2023) models are also implemented. To our knowledge, these are the first simulations of sooting flames with a finite-rate fusing model derived from a carbonaceous material. Moreover, while most simulations of the Santoro flame are limited to the non-smoking experiment, in the present work the incipient and smoking flames are simulated. A no-fusing model is also presented as a counter-example to the finite rate fusing scenarios. By investigating all three Santoro flames, the aim is to understand the role played by fusing across a variety of smoking conditions and the level of predictive power that is achievable with each fusing model with the two-PBE framework.

## 2. Soot aggregate fusing models

The majority of simulations of sooting flames do not account for finite-rate fusing. Instead, particles of a size smaller than a predefined cut-off value are assumed to fuse instantly and remain spherical. Above the cut-off size, fusing is assumed to be infinitely slow and aggregates form. The cut-off size accounts for the transition between spherical nuclei and larger aggregates and has to be empirically prescribed. This approach has been previously used within a univariate PBE framework (Liu et al., 2020; Liu & Rigopoulos, 2019; Sewerin & Rigopoulos, 2018; Sun & Rigopoulos, 2022).

**Table 1**
Summary of finite rate soot fusing timescale expressions.

| Fusing timescale model | $\tau_\sigma$ | $A_0$ | $T_a$ (K) | Source |
|---|---|---|---|---|
| Furnace black A | $A_0 d_p \exp(\frac{T_a}{T})$ | $1.2 \times 10^4$ | 5199 | O'Sullivan et al. (2025) |
| Furnace black B | $A_0 d_p \exp(\frac{T_a}{T})$ | $6.6 \times 10^1$ | 15,617 | O'Sullivan et al. (2025) |
| Ethylene prep. at 1600 K | $A_0 d_p^4 T \exp(\frac{T_a}{T})$ | $2.5 \times 10^{22}$ | 12,066 | Matsukawa et al. (2023) |
| Ethylene prep. at 1800 K | $A_0 d_p^4 T \exp\left(\frac{T_a}{T}\right)$ | $3.0 \times 10^{22}$ | 16,842 | Matsukawa et al. (2023) |

Fusing of primary particles within aggregates results in a reduction in the number of primary particles without any change in the overall number of aggregates or volume fraction. Therefore, an associated decrease in the average number of primary particles per aggregate and an increase the average primary particle diameter takes place. The rate of fusing is described by the following equation (Friedlander & Wu, 1994), which describes fusing a surface area minimisation process:

$$\left.\frac{\partial n_p(v)}{\partial t}\right|_{\text{fusing}} = -\frac{3}{\tau_\sigma}(n_p - n_p^{2/3}) \tag{1}$$

where $n_p(v)$ is the primary particle volume distribution and $\tau_\sigma(d_p, T)$ is the characteristic fusing timescale. The main challenge in developing a fusing expression lies in providing a model for the timescale that reflects the properties of the particular material. So far, this approach has been implemented in few sooting flame simulations, with the timescale expression being based on non-carbonaceous materials whose sintering law is well studied, such as silica (Chen et al., 2013; Sun et al., 2021) and titania (Sun et al., 2021; Veshkini et al., 2016). The significance of the recent carbonaceous-based fusing timescale models of Matsukawa et al. (2023) and O'Sullivan et al. (2025) is that they are based on the observed fusing behaviour of carbonaceous aggregates. Matsukawa et al. (2023) used the experimental results of the inert re-heating fusing experiment of Ono et al. (2017) to calibrate the activation temperature and pre-factor whilst initially assuming a fourth order dependency on primary particle diameter.

O'Sullivan et al. (2025) collated a large number of experimentally reported C/O (wt %) and C/H (wt %) ratios for a wide variety of carbon black grades and soot samples. Inferences were made as to which subset of carbon black grades could serve as a soot proxy. With the selection of carbon black grades narrowed down, their respective reactor data and observed reactor timescales allowed for systematic extraction of the expression for the fusing timescale, based on the inverse population balance approach. The latter can be used to model a collision-coalescence process with an unknown fusing timescale, but with known input and output conditions such as primary particle diameter and temperature. This allows the determination of both the form of scaling relationship and the values of the parameters that best fit the experimental data. Importantly, no initial assumption regarding the functional form of the scaling expression with respect to the primary particle diameter is required in this methodology. A linear scaling was determined to be the most thermodynamically suitable one, and subsequently, the activation temperature and pre-factor were obtained. More information on the inverse population balance approach used in that work can be found in Diemer (2023), while a related approach that considers simultaneous sintering and reaction can be found in Modi et al. (2023). As a validation case, O'Sullivan et al. (2025) simulated the re-heating experiment of Ono et al. (2017) with the new fusing models. That work serves as perhaps the only direct soot fusing experiment where other particulate processes were minimised or totally removed by design. Good agreement was found between the predicted fusing behaviour and experimental data.

An important aspect of fusing models is that the underlying mechanisms depend on the material properties of the particular aggregate. In the case of soot, its material properties are not well understood and a range of material behaviour has been observed from liquid-like to fully graphitised 'hard-shell' primary particles. This is why both Matsukawa et al. (2023) and O'Sullivan et al. (2025) presented two sets of fusing models each. Namely, one fusing model with a higher activation temperature for a more graphitic type of soot and one fusing model with a lower activation temperature indicating a less graphitic type. In O'Sullivan et al. (2025), this was accomplished by considering the composition of the carbon black samples used as soot proxies and distinguishing two main groups reflecting the greater and lesser degrees of graphitisation. The fuel used, temperature and residence time all affect the composition of soot, hence the use of these models involves an assumption of an average or most representative composition of the soot aggregates across the flames being simulated. The three different flames studied in the present work cover a range of smoking conditions and it is plausible that the soot produced may differ in composition in each case. This is reflected in the different performance of the models, and will be discussed in Section 7.

The various finite rate expressions are summarised in Table 1. It should be noted that, in the present work, the fusing model is employed for particles bigger than 5 nm, while smaller particles (nascent soot nuclei) are assumed to fuse instantaneously. Finally, as a counter example, a 'no-fusing' model will also be presented; this model represents the case of instant graphitisation above the cut-off size of 5 nm. After that, any changes in primary particle size can be attributed only to surface growth and oxidation. While this is not realistic, as it corresponds to an infinitely high activation temperature once aggregates form, it will serve as a limiting case for comparison purposes.

## 3. The two-PBE formulation for aggregates

The two-PBE approach adopted in the present paper is in the form presented by Sun et al. (2021), while more information can be found in Rigopoulos (2024). It consists of one PBE for the evolution of the number density of soot particles, $n(v)$, which may be incipient spherical particles or aggregates, and another PBE for the number density of primary particles within aggregates of volume $v$, $n_p(v)$. In the following, $v$ refers to the volume of an aggregate and is the sum of the volumes of all primary particles; hence it is not equivalent to typical experimentally observable quantities such as aggregate collision diameter, mobility diameter, and radius of gyration. Below a cut-off size, the particles are all primary and therefore both distributions are identical. This cut-off size is chosen to distinguish the very small incipient soot particles that fuse instantaneously from the aggregates which experience finite rate fusing. The ratio of the two distributions represents the average number of primary particles per aggregate for a given aggregate size, $n_{av}(v)$, as shown below:

$$n_{av}(v) = \frac{n_p(v)}{n(v)} \tag{2}$$

which is related to the volume of aggregates ($v$) and of primary particles ($v_p$) as follows:

$$n_{av}(v) = \left(\frac{v}{v_p}\right) \tag{3}$$

Another relationship involves the diameter of gyration of an aggregate (Sorensen, 2011) and that will become important when considering the aggregation kernel is the following:

$$n_{av}(v) = k_f \left(\frac{d_g}{d_p}\right)^{D_f} \tag{4}$$

where $D_f$ and $k_f$ are the fractal dimension and pre-factor, respectively. Note that, in the simple case of spherical particles, $n_p(v)$ and $n(v)$ are equal, and $n_{av}(v)$ collapses to 1. It is common to consider the fractal dimension to be constant throughout any given sooting flame and this aspect of soot aggregates has been observed experimentally (Gwaze et al., 2006; Köylü et al., 1995, 1997; Link et al., 2011; Schenk et al., 2015). If collisions between aggregates are faster than the fusing within aggregates then the fractal dimension is effectively pinned at a constant value. This can be thought of as the limiting case of diffusion-limiting aggregation (Meakin, 1983, 1987; Sorensen & Roberts, 1997). This effect has been seen across flame generated inorganic aggregates and simulation studies (Kruis et al., 1993; Tsantilis et al., 2002; Tsantilis & Pratsinis, 2000). Koch and Friedlander (1989) reinforces the idea that fusing acts to reduce the surface area regardless of fractal dimension. The mass fractal dimension for soot aggregates has been measured to lie in a narrow range around 1.8, and previous simulation studies have used this value across both laminar and turbulent sooting flames (Dworkin et al., 2011; Liu & Rigopoulos, 2019; Saggese et al., 2015; Sun & Rigopoulos, 2022; Sun et al., 2021; Zhang et al., 2009). Thus, soot aggregates are described with a constant fractal dimension of 1.8 and corresponding pre-factor, $k_f$, of 1.94 (Link et al., 2011) throughout the present work.

The two PBEs are shown below, while details regarding their derivation can be found in Rigopoulos (2024).

$$\begin{aligned}\frac{\partial n}{\partial t} + \frac{\partial [Gn]}{\partial v} + \frac{\partial (u_j n)}{\partial x_j} =& \frac{\partial}{\partial x_j}\left(D_p \frac{\partial n}{\partial x_j}\right) + \dot{B}(Y_\alpha)\delta(v - v_{nuc}) + \dot{C}(Y_\alpha) \\ &+ \frac{1}{2}\int_0^v \beta(w, v-w)\, n(w)\, n(n(v-w)\, dw - \int_0^\infty \beta(v, w)\, n(v)\, n(w)\, dw\end{aligned} \tag{5}$$

$$\begin{aligned}\frac{\partial n_p}{\partial t} + \frac{\partial [G \cdot n_p]}{\partial v} + \frac{\partial (u_j n_p)}{\partial x_j} =& \frac{\partial}{\partial x_j}\left(n_{av} D_p \frac{\partial n}{\partial x_j}\right) - \frac{3n}{\tau_\sigma}\left[\frac{n_p}{n} - \left(\frac{n_p}{n}\right)^{2/3}\right] + \dot{C}_p(Y_\alpha) \\ &+ \frac{1}{2}\int_0^v \beta(w, v-w)\, n(w)\, n(n(v-w)\left[n_{av}(v-w) + n_{av}(w)\right] dw \\ &- \int_0^\infty \beta(v, w)\, n(v)\, n(w)\, n_{av}(v) dw\end{aligned} \tag{6}$$

## 4. Soot kinetic models

### 4.1. Chemical reaction mechanism

In order to account for the generation of soot precursors in a consistent manner regarding the nucleation and surface growth kinetics, the detailed chemical reaction mechanism of Blanquart et al. (2009) is employed. Accounting for 149 species across 1651 elementary reactions, this reaction mechanism is capable of describing the formation of large PAH molecules up to cyclopenta[cd]pyrene ($C_{18}H_{10}$). The mechanism has been validated for various fuels with increasing carbon numbers — from methane up to iso-octane. Equally, various flame types and burners have been used to test the chemical kinetics of this mechanism, ranging from laminar premixed to counter-flow diffusion flames.

### 4.2. Aggregation

The collision frequency function, $\beta(v,w)$, appears in the integral birth and death terms accounting for aggregation. The collision rate takes various forms depending on the Knudsen number involved - $Kn = \frac{2\lambda_f}{d}$ where $\lambda_f$ is the gas mean free path and $d$ is particle collision diameter. Three regimes are relevant here: the free-molecular regime where soot particles collide with each other at a similar rate to which gas-phase species collide with themselves, the continuum regime where larger soot aggregates collide less frequently than the gas-phase species and view the surrounding gas molecules as a continuum, and the transition regime in between where a hybrid collision kernel is considered (Kazakov & Frenklach, 1998; Pratsinis, 1988). The expressions are:

$$\beta_{fm}(v,w) = E_f\sqrt{\frac{\pi k_b T}{2\rho_s}}\left[\frac{1}{v}+\frac{1}{w}\right]^{\frac{1}{2}}(d(v)+d(w))^2; \qquad \mathrm{Kn} < 0.1$$

$$\beta_c(v,w) = \frac{2k_bT}{3\mu}\left[\frac{Cu(v)}{d(v)}+\frac{Cu(w)}{d(w)}\right](d(v)+d(w)); \qquad \mathrm{Kn} > 10$$

$$\beta_t(v,w) = \frac{\beta_{fm}\,\beta_c}{\beta_{fm}+\beta_c}; \qquad 0.1 < \mathrm{Kn} < 10 \tag{7}$$

where $Cu(v)$ is the Cunningham slip correction factor given by $Cu(v) = 1+1.257\mathrm{Kn}(v)$ and $d(v)$ is the collision diameter of an aggregate of size $v$ taken to be equal to the diameter of gyration in Eq. (4). Oh and Sorensen (1997) presents a detailed discussion regarding the collision diameter, gyration diameter, and mobility diameter of an aggregate and finds it is reasonable to approximate these three aggregate sizes as equal when describing soot aggregate collision rates. Maricq (2007) further confirms this approach by successfully modelling the soot collision dynamics in the absence of nucleation, surface growth and oxidation. Note that, for spherical particles beneath the cut-off size the volume $v$ can be readily converted into a collision diameter without the need for the fractal relations in Eq. (4). More recent approaches to the modelling of collisions between aggregates have appeared, including Karsch and Kronenburg (2023), Karsch et al. (2022) and Thajudeen et al. (2012), but in the present work the main objective is to assess the effect of fusing as described by a model derived from a carbonaceous material. Therefore, with respect to the other elements of the simulation, so we have opted to retain the modelling approach that was used by Sun et al. (2021) (which however employed fusing laws derived from silica and titania).

### 4.3. Surface growth and oxidation

Surface growth and oxidation rates are calculated via the Hydrogen-Abstraction Acetylene-Addition (HACA) scheme of Blanquart and Pitsch (2009a). First proposed by Frenklach and Wang (1991), the HACA framework states that the loss of hydrogen from a surface C-H bond produces a radical site, which in turn acetylene molecules readily react with — adding two new carbon atoms to the surface of the soot particle. A series of surface reactions valid for an individual active site were derived, with the corresponding rate equations estimated via analogous gas-phase reactions involving simple aromatic molecules such as benzene and phenyl. Blanquart and Pitsch (2009b) formulated a set of rate coefficients as modified Arhenius' laws, compiling previous results across reactions involving acetylene (Tokmakov & Lin, 2004), H (Harding et al., 2005; Mebel et al., 1997), OH (Tokmakov & Lin, 2002) and oxidation reactions (Kazakov et al., 1995; Neoh, 1980). Table 2 presents the HACA scheme implemented in the current work. Note that reaction rate no. 6 is derived empirically as being proportional to the available soot surface area and scales with the square root of the local temperature (Neoh, 1980).

**Table 2**
Summarised HACA elementary surface reactions (Blanquart & Pitsch, 2009a) in modified Arhenius form: $k = AT^n\exp(\frac{-E_a}{RT})$. Units are $cm^3$, mol, s, and kJ.

| | No. | Reaction | | | A | n | $E_a$ |
|---|---|---|---|---|---|---|---|
| Growth | 1 | $C_{(s)}$-H + H | ⇌ | $C_{(s)}\cdot$ + $H_2$ | $1.00\times10^{8}$8.68 × $10^{4}$ | 1.802.36 | 68.4225.46 |
| | 2 | $C_{(s)}$-H + OH | ⇌ | $C_{(s)}\cdot$ + $H_2O$ | 6.72 × $10^{1}$6.44 × $10^{-1}$ | 3.333.79 | 6.0927.96 |
| | 3 | $C_{(s)}\cdot$ - H | ⇌ | $C_{(s)}\cdot$ + H | 1.13 × $10^{16}$4.17 × $10^{13}$ | −0.060.15 | 476.050.00 |
| | 4 | $C_{(s)}\cdot$ +$C_2H_2$ | → | $C_{(s)}$ - H + H | 2.52 × $10^{9}$ | 1.77 | 13.54 |
| Oxidation | 5 | $C_{(s)}\cdot$ + $O_2$ | → | $C_{(s)}$-H + 2 CO | 2.20 × $10^{12}$ | 0.0 | 31.38 |
| | 6 | $C_{(s)}$ - H +OH | → | $C_{(s)}$-H +CO | Reaction probability 0.13 | | |

Next, an estimation has to be made regarding the total number of active sites available to react. Under the HACA perspective this quantity is represented by the product of a maximum site surface density $\chi_H$, and the proportion of sites which are actively participating, $\alpha$. Considerable uncertainty surrounds the surface reactivity parameters that govern the effective surface density of

reactive sites. Since fusing is the focus of this study, the surface reactivity parameters were taken from Sun et al. (2021). Namely, the proportion of active sites were calculated via the Arhenius law of Guo et al. (2006), with the maximum surface density of hydrogenated sites taken to be $\chi_H = 2.3 \times 10^{19}$ sites/m$^2$ and viewed as constant throughout. Using the per-site rates, and an estimation of the total number of sites per unit surface area of soot aggregate, a mass growth rate per unit surface area is found, $\dot{R}(Y,T)$. Finally, the mass growth rate predicted by the HACA scheme is related to the surface growth law $G(\mathbf{Y},v)$ found in the PBE (Eqs. (5) & (6)):

$$G(\mathbf{Y},v) = \frac{a(v)}{\rho_s}\dot{R}(\mathbf{Y},T) \tag{8}$$

Where a(v) is the surface area of aggregates of size v, and $\rho_s$ is the density of soot, taken to be 1860 kg/m$^3$ (Purl et al., 1993). The surface area of a soot aggregate was evaluated using the empirically derived relationships of Brasil et al. (1999), Eq. (9).

$$a(v) = a_{(C_{ov}=0)}\left[1 - \phi_a C_{ov}\left(1 - \frac{1}{n_{av}(v)}\right)\right] \tag{9}$$

Where $\phi_a$ is the average number of contacts per primary particle and is taken to have a value of 1.3, $C_{ov}$ is overlap parameter and a value 0.15 was used, and $a_{(C_{ov}=0)}$ is the surface area of an aggregate with point contact between primary particles. Note that, if the $n_{av}$ happens to be 1, as is the case for spherical particles, then Eq. (9) collapses to give the surface area of a sphere.

### 4.4. Nucleation and condensation

#### 4.4.1. Dimer balance

Nucleation and condensation rates are described via the collision kinetics of precursor dimers as presented in Blanquart and Pitsch (2009a). A collection of Polycyclic Aromatic Hydrocarbon (PAH) gas-phase species are said to self-collide and form dimers, an intermediate species between the gas phase and the solid nuclei. Dimers are considered intermediate species due to their short lifetimes, less than ≈ 20 ps. Once dimers have formed, the subsequent collision between dimers or *self-dimerisation* is said to nucleate solid particles. Similarly, condensation occurs when dimers collide with existing solid particles, either incipient soot or aggregates. Nucleation and condensation both consume dimers and one key assumption is that a quasi-equilibrium forms due to the high collision rate for both process. A quadratic equation in terms of dimer concentration forms, that balances the production of dimers due to PAH self-collision with the consumption of dimers due to nucleation and condensation:

$$b_{\text{nuc}}[dimer]^2 + c_{\text{cond}}[dimer] = \sum_{\xi=1}^{8}\dot{\omega}_\xi \tag{10}$$

Eight PAH species are considered, ranging from naphthalene ($C_{10}$ $H_8$) to cyclopenta[cd]pyrene ($C_{18}H_{10}$) and the self-collision rate for PAH species $\xi$, as the number of collisions per unit volume of carrier gas per second, is given as:

$$\dot{\omega}_\xi = \gamma_\xi\sqrt{\frac{4\pi k_B T}{m_\xi}}\, d_\xi^2\,[\text{PAH}_\xi]^2\, N_A^2 \tag{11}$$

$$d_\xi = D_A\sqrt{\frac{2N_C(\xi)}{3}} \tag{12}$$

where $\gamma_\xi$ is the sticking coefficient for PAH$_\xi$, $N_A$ is the Avogadro's constant, $k_B$ is the Boltzmann constant, $m_\xi$ is the mass of PAH$_\xi$, and $d_\xi$ is the molecule diameter of PAH$_\xi$ given in Eq. (12). Note that $D_A$ is the size of a single aromatic ring taken as $1.395\sqrt{3}$ Å, and $N_C(\xi)$ is the number of carbon atoms in the given PAH molecule $\xi$. When all eight PAH species are considered, Eq. (11) gives the rate of dimer production, as one successful self-collision leads to the production of a dimer and the consumption of two PAH molecules. No distinction is made between different types of dimers originating from different PAH species, as it is the total concentration of dimers that drives nucleation and condensation.

#### 4.4.2. Nucleation kinetics

The free-molecular collision rate of two dimer molecules is given by Eq. (13), and leads to the nucleation of an assumed spherical soot particle.

$$\dot{\omega}_{nuc} = E_F\left(\frac{3}{4\pi}\right)^{1/6}\sqrt{\frac{6k_B T}{\rho_s}}4\sqrt{2}V_{\text{Dim}}^{\frac{1}{6}}[\text{Dimer}]^2 N_A^2 \tag{13}$$

Where $E_F$ is an enhancement factor due to Van der Waal forces (Harris & Kennedy, 1988) that is equal to 2.2 and $V_{\text{Dimer}}$ is a weighted average Dimer volume, Eq. (14). Essentially, all different dimer sizes are approximated by the average in Eq. (14), although differences in local composition can lead to a different average dimer volume.

$$V_{\text{Dim}} = \frac{\sum \omega_\xi 2V_\xi}{\sum \omega_\xi} \tag{14}$$

Finally, the nucleation source term in Eq. (5) can be equated via the following integral relationship assuming new particles are added at the nucleation size $v_{nuc}$ equal to $2V_{\text{Dim}}$:

$$\int_0^\infty \dot{B}\ \delta(v - v_{nuc})dv = \dot{\omega}_{nuc} \tag{15}$$

This subtle distinction is due to the fact that the nucleation kinetics are defined in terms of the rate of new particles being produced, as opposed to the rate of change of the size distribution directly. For completeness, the coefficient $b_{nuc}$ can be evaluated the following relation:

$$b_{nuc} = 2\frac{\dot{\omega}_{nuc}}{[\text{Dimer}]} \tag{16}$$

#### 4.4.3. Condensation kinetics

Condensation is viewed as the successful collision between a dimer molecule and an existing soot particle, and adds the volume $V_{\text{Dim}}$ to the soot particle increasing its size. The rate of collision between dimers and soot aggregates in the size range $v$ to $v + dv$ is given as:

$$\dot{\omega}_{\text{cond}}(v)\, dv = \beta_{\text{cond}}[\text{Dimer}]\ N_A\ n(v)\, dv \tag{17}$$

where $\beta_{\text{cond}}$ is the collision frequency between dimers and soot particles and takes a free-molecular form:

$$\beta_{cond} = A_F\sqrt{\frac{\pi k_b T}{2\rho_s}}\left(d_{\text{Dim}} + d(v)\right)\sqrt{\frac{1}{V_{\text{Dim}}} + \frac{1}{v}} \tag{18}$$

where $A_F$ is the amplification factor due to van der Waals interactions and taken to be 1.3 (Marchal, 2008). Next it is assumed that each successful collision leads to the condensation of a dimer molecule, hence the soot particle volume increases by $V_{\text{Dim}}$. The condensation rate is kinetically formulated in terms of the rate of successful collisions leading to the addition of mass on the surface of soot particles. The condensation term in Eq. (5) can be related to this mass-addition point of view via the following relation:

$$\dot{C}(v, Y_\alpha)\, v\, dv = \dot{\omega}_{\text{cond}}(v)\, V_{\text{Dim}}\, dv \tag{19}$$

Finally, when considering the total number of dimers consumed by condensing on all possible soot particles, $c_{\text{cond}}$ (Eq. (10)) can be evaluated to complete the dimer balance as follows:

$$c_{\text{cond}} = \frac{\int_0^\infty \dot{\omega}_{\text{cond}}(v)\, dv}{[\text{Dimer}]} \tag{20}$$

## 5. Coupling of PBE with flow

The transport of soot particles in physical space is described via the convection and diffusion terms, and Eqs. (5) & (6) are repeated in a simplified form where all internal processes are absorbed into a source term and the external processes left in their original forms:

$$\frac{\partial n}{\partial t} + \frac{\partial (u_j n)}{\partial x_j} = \frac{\partial}{\partial x_j}\left(D_p \frac{\partial n}{\partial x_j}\right) + \dot{S}\ (v, Y_\alpha) \tag{21}$$

$$\frac{\partial n_p}{\partial t} + \frac{\partial (u_j n_p)}{\partial x_j} = \frac{\partial}{\partial x_j}\left(n_{av} D_p \frac{\partial n}{\partial x_j}\right) + \dot{S}_p(v, Y_\alpha) \tag{22}$$

As is customary in CFD solvers, the physical transport is separated from reaction (source) terms via the fractional step method. Considering the first fractional step containing only contributions due to convection–diffusion in physical space, as well as integrating across the interval $\Delta v_i$ in particle volume space: Eqs. (21) & (22) represent the transport in physical space of both discretised particle size distributions. Detailed treatment and verification of this approach can be found in Appendix A of Sun et al. (2021).

$$\left.\frac{dn_i}{dt}\right|_{\text{con-diff}} + \frac{\partial (u_j n_i)}{\partial x_j} = \frac{\partial}{\partial x_j}\left(D_p \frac{\partial n_i}{\partial x_j}\right) \tag{23}$$

$$\left.\frac{dn_{p,i}}{dt}\right|_{\text{con-diff}} + \frac{\partial (u_j n_{p,i})}{\partial x_j} = \frac{\partial}{\partial x_j}\left(n_{av,i} D_p \frac{\partial n_i}{\partial x_j}\right) \tag{24}$$

where $u_j$ is the velocity, which takes into account the thermophoretic velocity caused local temperature gradients (Friedlander, 2000) as well as the flow velocity, $U_j$. This relationship is shown in Eq. (25), where $\mu$ is the gas dynamic viscosity, and $\rho$ is the gas density.

$$\begin{aligned} u_j &= U_j + u_j^t \\ \text{where } u_j^t &: \\ u_j^t &= -0.55\frac{\mu}{\rho T}\frac{\partial T}{\partial x_j} \end{aligned} \tag{25}$$

**Table 3**
Summary of CFD Solver Numerical Schemes.

| Process | Spatial discretisation | Internal discretisation | Temporal discretisation |
|---|---|---|---|
| Convection-Diffusion | TVD scheme (van Leer limiter)<br>Central Difference (2nd-order) | – | Crank–Nicolson (2nd-order) |
| Chemical Reaction | – | – | Implicit Euler<br>Modified Newton–Raphson |
| Discretised 2PBE | – | see Section 6 | Explicit Euler<br>dopri (Hairer et al., 1993) |

## 6. Numerical formulation of two-PBE discretisation schemes

In order to discretise $n(v)$ and $n_p(v)$, a piecewise constant approximation is used. The aggregation terms are solved numerically via the mass conservative scheme of O'Sullivan and Rigopoulos (2022) and Liu and Rigopoulos (2019).

Thus, the second fractional step containing contributions from all internal processes can be assembled as follows:

$$\left.\frac{dn_i}{dt}\right|_{\text{Internal}} = \left.\frac{dn_i}{dt}\right|_{growth} + \dot{B}_i + \dot{C}_i(v, Y_\alpha) + \left.\frac{dn_i}{dt}\right|_{\text{Agg}} \tag{26}$$

$$\left.\frac{dn_{p,i}}{dt}\right|_{\text{Internal}} = \left.\frac{dn_{p,i}}{dt}\right|_{growth} + \dot{C}_{p,i}(v, Y_\alpha) + \left.\frac{dn_{p,i}}{dt}\right|_{\text{Agg}} - \frac{3}{\tau_\sigma}\left[\frac{n_{p,i}}{n_i} - \left(\frac{n_{p,i}}{n_i}\right)^{2/3}\right] n_i \tag{27}$$

An optically thin radiation model is used, and its implementation is described in Sewerin and Rigopoulos (2018).

### 6.1. Implementation in CFD flow solver

The two-PBE approach describing soot aggregates was implemented in the in-house CFD code: BOFFIN (Jones et al., 2002). BOFFIN employs a second-order finite volume scheme in physical space to discretise all scalars, and uses a separate fractional step for convection–diffusion, the reaction of chemical species, and the internal processes relating to the PBE. A brief summary of the various integration schemes used in BOFFIN are presented in Table 3.

Note that, due to the stiff system of non-linear equations that appear in the chemical reaction fractional step, a stiff solver had to be used that uses a joint implicit Euler and modified Newton–Raphson scheme. Finally, the two-PBE fractional step where the internal particulate processes are integrated in time was found to not be numerically stiff, and explicit methods can be used. Considering the particulate fractional step, the explicit Euler solver was used for the two-PBE for the majority of timesteps ($\approx 3$ flow-through times). However, to confirm that convergence had been reached, the solution continued to run using the dopri solver. The dopri solver is another explicit solver, but has a dynamic timestep adjustment scheme should the temporal integration not be fully converged. When dopri was used on the final timesteps ($\approx 1$ flow-through time) of all flame simulations, it was found that the dynamic timestep adjustment algorithm was not called. This indicates that the overall solution had indeed converged.

### 6.2. CFD set-up and modelling of Santoro flames

The Santoro flames are laminar axisymmetric co-flow ethylene flames (Santoro et al., 1987). The axisymmetric geometry allows for modelling them using a cylindrical two-dimensional mesh in the r-z plane. The central fuel jet has a diameter of 11.1 mm, and the outer concentric air flow has a diameter of 101.6 mm. The air is taken to be at atmospheric pressure with a temperature of 300 K. The inlet velocity profiles are assumed to be uniform, and this was achieved experimentally via the use of glass beads (Santoro et al., 1987) in the fuel and air channels. There exists a degree of uncertainty regarding the inlet temperature and the extent of fuel preheating. Better predictions can be obtained by increasing the fuel inlet temperature (Guo et al., 2002) and several studies have followed this approach (Dworkin et al., 2011; Veshkini et al., 2016). In the present work, we have adopted the same approach as in our earlier work (Sun et al., 2021) where no preheating was applied, in order to facilitate comparisons with that work and focus on the effect of fusing.

The computational domain is discretised into 20,000 cells, with 100 cells spanning the radial direction and 200 cells spanning the axial direction. Moreover, grid stretch factors of 1.03 and 1.01 are applied in the radial and axial directions respectively, in order to increase the mesh resolution towards the centreline and inlet. Sun et al. (2021) tested successive grid refinements to prove a grid independent solution, and found that 20,000 cells sufficed.

The different inlet conditions across the three variations of the Santoro flame are summarised in Table 4. Santoro et al. (1983) comments that observed flame length in the non-smoking case was approximately 88 mm, and that increasing the fuel flow rate leads to an increase in observed flame length and residence times available for particle growth (Santoro et al., 1987). The fuel and air inlet velocities in Table 4 were implemented in three distinct CFD simulations.

## 7. Results and discussion

Results for all three Santoro flames will be presented in this section, starting with the non-smoking flame, and then moving to the incipient smoking and smoking ones.

**Table 4**
Summary of inlet conditions across variants of Santoro flame experiments.

| | Fuel volumetric flow rate ($cm^3 s^{-1}$ | Fuel inlet velocity ($cm\ s^{-1}$) | Air volumetric flow rate ($cm^3\ s^{-1}$) | Air velocity ($cm\ s^{-1}$) |
|---|---|---|---|---|
| Non-smoking (NS) | 3.85 | 3.98 | 713.3 | 8.90 |
| Incipient Smoking (IS) | 4.60 | 4.75 | 713.3 | 8.90 |
| Smoking (S) | 4.90 | 5.05 | 1068.3 | 13.3 |

### 7.1. Non-smoking flame

#### 7.1.1. Soot volume fraction

Fig. 1(a) shows the three carbonaceous-based fusing models predicting similar levels of integrated soot volume fraction early in the non-smoking flame. Soot volume fraction generation is dominated by surface growth and oxidation, and this effect is confirmed by the contributions shown in Fig. 2(a) . Note the various scales across Figs. 2(a) 2(c) 2(b) where growth contributes roughly 10 times the volume fraction versus condensation, and 100 times the volume fraction which nucleation contributes. With HAB less than 0.05 m, the carbonaceous-based models overpredict the total quantity of soot present in the flame reaching a shared peak consistent with the experimentally observed maximum value, albeit at a lower HAB. This structural 'shift' of integrated volume fraction towards the inlet can be explained by considering the large uncertainty surrounding inlet preheating. Essentially, although the fuel inlet is nominally reported as 300 K experimentally, once the flame is established heating of the inlet tube can occur raising the inlet temperature. The inlet temperature is not measured directly, hence the uncertainty on what the true inlet condition should be in simulations. As mentioned in Section 6.2, it is common for simulations of the Santoro flame to include preheating effects by raising the inlet temperature. As the main aim of this study is to explore the role of fusing, we have adopted the same approach as in our earlier work (Sun et al., 2021) to which the present work is to be juxtaposed and where no preheating was applied, hence discrepancies near the nozzle are to be expected.

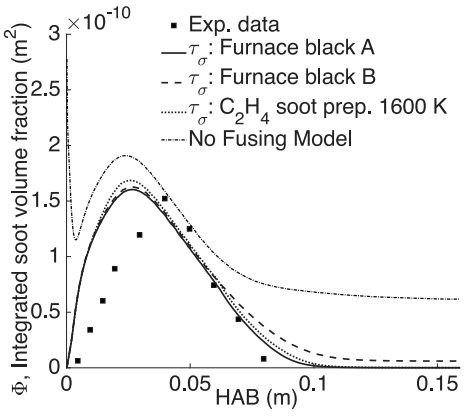


(a) Integrated soot volume fraction (Santoro et al., 1987).

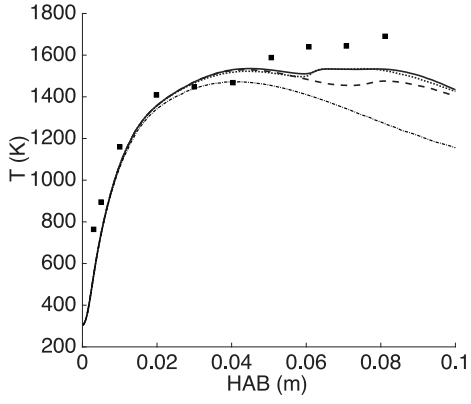


(b) Centreline temperature, (Köylü et al., 1997; Santoro et al., 1987).

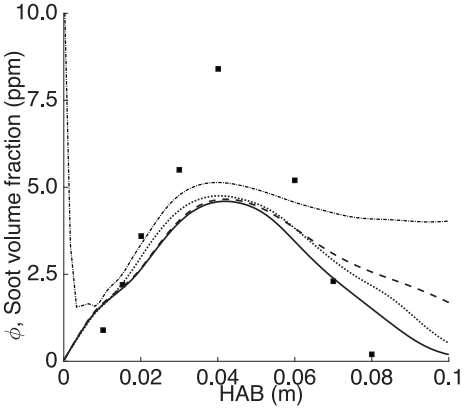


(c) Soot volume fraction along path of maximum soot, light extinction data compiled from Santoro et al. (1983, 1987).

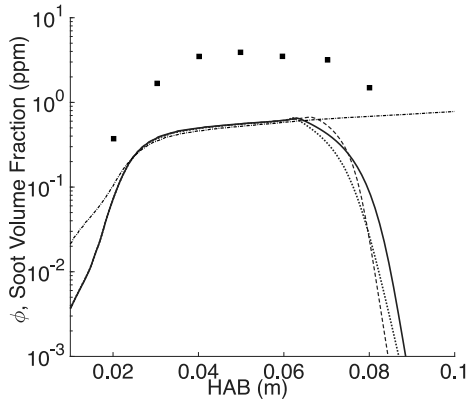


(d) Centreline soot volume fraction, from (Köylü et al., 1997).

**Fig. 1.** Non-smoking flame soot volume fraction and temperature results.

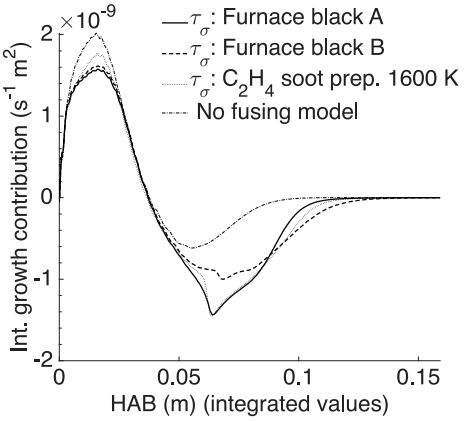


(a) Integrated surface growth/oxidation contribution to volume fraction.

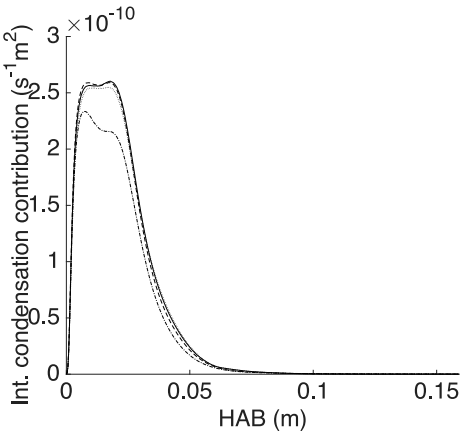


(b) Integrated condensation contribution to volume fraction.

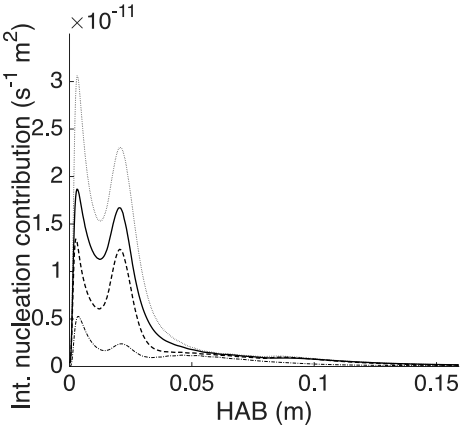


(c) Integrated nucleation contribution to volume fraction.

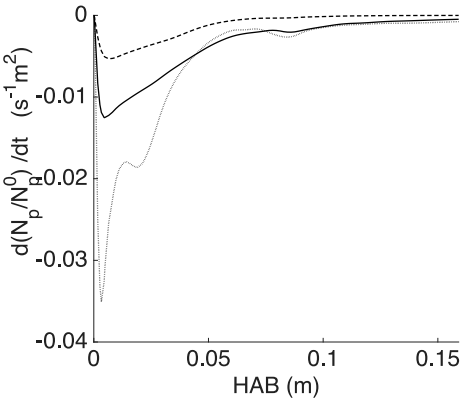


(d) Integrated normalised rate of primary particle loss due to fusing.

**Fig. 2.** Growth, condensation, nucleation, and fusing contributions in the non-smoking flame.

Notably, when fusing is ignored, very different behaviour is simulated early on in the flame. A burst of soot generation is seen close to inlet, with the integrated soot volume fraction then dropping rapidly to largely follow the same profile as the other simulations, albeit shifted to higher levels of soot relative to the finite rate fusing models. Clearly, without fusing there is increased surface area with equivalent temperature and surface growth is overpredicted. It is in this initial region that fusing in the carbonaceous-based models is at its most intense, as shown by the normalised rate of primary particle loss, Fig. 2(d) . Note that the no fusing model does not remove primary particles due to fusing by definition and its results are not plotted in Fig. 2(d) .

Two distinct types of burnout behaviour are seen across Fig. 1(a) & 1(c). Furnace black A and ethylene-based soot fusing models correctly predict total burnout whilst furnace black B and the model predict soot release at exit. At HAB greater than 0.05 m oxidation is expected to become the dominant surface reaction and clearly the relative surface area available as well as temperature play a role in determining oxidation rates. Fig. 2(a) also confirms that oxidation (negative growth) contributions differ according to fusing model, with furnace black B and the model having significantly less oxidation removing volume fraction beyond HAB = 0.05 m. Fig. 2(d) further shows that the normalised fusing rate with furnace black B essentially reduces to zero beyond HAB = 0.05 m, whereas the furnace black A and the ethylene-soot based model still show a meaningful amount of fusing at around HAB = 0.1 m. Clearly, aggregate fusing and the resultant surface area have significant consequences in the burnout region and an in-depth mechanistic explanation is given in Section 7.1.2.

One final effect is the role of radiative heat losses which are modelled as being proportional to soot volume fraction. Clearly, the fusing models that fail to remove volume fraction via oxidation fast enough begin to lose temperature as the increased level of remaining soot volume fraction leads to higher radiative losses. This reinforcing loop acts to further reduce oxidation rates and is most obvious in the model temperature profile (Fig. 1(b)) and to a smaller extent in the furnace black B profile around HAB 0.07 m.

Fig. 1(d) shows an underprediction of roughly an order of magnitude of volume fraction relative to experimental data across all fusing models. This underprediction has been seen in the works of Dworkin et al. (2011) and Sun et al. (2021). Soot volume fraction generation along the centreline has been mainly attributed to nucleation and condensation processes (Sun et al., 2021; Veshkini et al., 2014). Whilst the two-PBE framework and fusing models primarily improve surface area and morphological predictions and thus aid

in predicting surface reactions correctly, the centreline is not dominated by surface growth. Instead, PAH precursor related processes are the main drivers of soot volume generation along the centreline. This underprediction is clearly not a function of fusing model and instead the current soot kinetics governing nucleation, condensation, and precursor generation may be underpredicting the soot volume fraction along the centreline. Moreover, Fig. B.14 (Appendix B) shows very little variation in the total number density and total PAH and benzene mole fraction along the centreline. This lack of difference between the various simulations confirms that the centreline soot volume fraction underprediction cannot be attributed to the chosen fusing model. Fig. 1(c) also shows considerable underprediction along the path of maximum soot, but in this case the discrepancy can be explained via the analysis of the varying refractive index of soot aggregates when inverting light extinction measurements (Kelesidis & Pratsinis, 2022). Morphology and composition can affect the refractive index of soot aggregates, and early studies assumed a constant refractive index throughout the Santoro flame to invert light extinction measurements into volume fraction readings. However, the above authors were able to show that when the evolving refractive index is modelled, light extinction derived volume fraction readings align with TPD probe measurements, and actually show a peak volume fraction of roughly 5 ppm (Kelesidis & Pratsinis, 2022). Unlike the centreline, volume fraction along the path of maximum soot is highly dependent on surface growth and, when the refractive index of soot aggregates is correctly accounted for, the simulation results across the carbonaceous-based models are overall inline.

### *7.1.2. Burnout behaviour*

To examine why specifically furnace black B and the no-fusing model do not burnout fully, radial distributions at the flame tip (HAB = 88 mm) of soot surface area, temperature, OH and $O_2$ mole fractions, and volume fraction oxidation rates have been plotted (Figs. 3(a)–3(d)). Comparing furnace black A and furnace black B results directly, Fig. 3(a) shows relatively similar temperature distributions but a marked difference in surface area. Furnace black B shows a peak soot surface area of 713 $m^2m^{-3}$ whereas furnace black A has a peak surface area of 165 $m^2m^{-3}$, with both distributions centred around r = 2 mm. Also, both distribution are roughly 2 mm wide, spanning from r = 1 mm to r = 3 mm. A drastically larger surface area should be favourable regarding burnout, yet despite this furnace black B does not burnout fully. Next, Fig. 3(b) reveals similar $O_2$ mole fraction distributions across furnace black A & B results, but dramatically different OH distributions. Namely, furnace black B appears to be nearly starved of OH at roughly r = 2 mm, whereas furnace black A only shows a small reduction in OH at r = 2 mm compared to OH levels at r = 3 mm. With reference to Table 2 and reactions 5 and 6: clearly a lack of OH, a sis the case with the furnace black B model, is strictly unfavourable with regards to oxidation and burnout

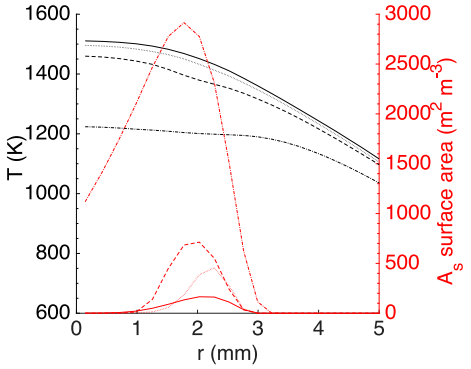


(a) Radial temperature and surface area distribution at the flame tip (HAB = 88 mm).

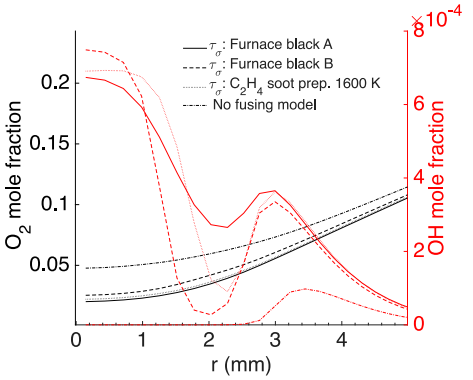


(b) $O_2$ and OH radial distributions at the flame tip.

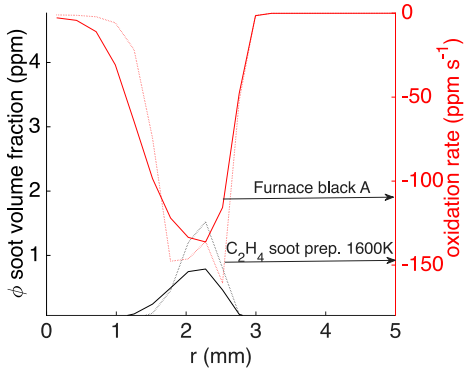


(c) Volume fraction and oxidation rate for furnace black A (solid line) and ethylene-based soot prep. 1600 K (dotted line) fusing models.

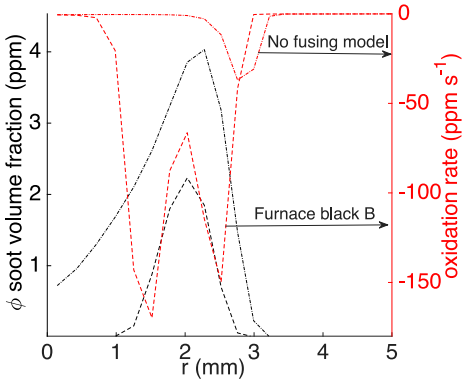


(d) Volume fraction and oxidation rate for furnace black B (dashed line) and no-fusing (dot-dash line) models.

**Fig. 3.** Radial profiles at the flame tip (HAB = 88 mm) for the non-smoking flame.

**Table 5**
Timescales in the reaction zone, Note surface areas and temperatures are radial averages across the reaction zone in Fig. 3(a).

| Fusing model | Surface area ($m^2m^{-3}$) | T (K) | $\tau_{OH}$ (ms) | $\tau_D$ (ms) | Comment |
|---|---|---|---|---|---|
| Furnace black A | 85 | 1450 | 8.5 | 3.4 | $\tau_D < \tau_{OH}$: Burnout |
| Furnace black B | 314 | 1395 | 2.4 | 3.6 | $\tau_D > \tau_{OH}$: OH starvation |
| Ethylene-based soot 1600 K | 157 | 1437 | 4.6 | 3.5 | $\tau_D < \tau_{OH}$: Burnout |
| no-fusing model | 1500 | 1225 | 0.6 | 4.3 | $\tau_D > \tau_{OH}$: OH starvation |

Fig. 3(c) shows the radial distribution for the volume fraction oxidation rate for furnace black A, and a unimodal shape is achieved with a peak oxidation rate of −136 ppm $s^{-1}$ centred at r = 2 mm. However, Fig. 3(d) shows the same distribution for furnace black B, and clearly at r = 2 mm a local minimum is produced with an oxidation rate of only −66 ppm $s^{-1}$. As r = 2 mm corresponds to where the majority of the soot volume fraction is centred, it is unsurprising that furnace black B is unable to fully burnout. Despite a larger surface area for a roughly equivalent temperature distribution, the sheer lack of OH where the majority of the soot is present prevents furnace black B from burning out as compared to furnace black A.

To further explain this OH starvation effect, it is necessary to consider to the timescales of the two competing processes of oxidation via OH and OH diffusion. With reference to reaction 6 in Table 2, the timescale for OH consumption is:

$$\tau_{OH} = \frac{1}{0.13\sqrt{\frac{RT}{2\pi M_{r,OH}}}\,A_s} \tag{28}$$

Note that $\tau_{OH}$ is independent of the local OH concentration, as is expected for what is effectively a first order reaction and crucially scales with inverse soot surface area $A_s$. Thus, a larger surface area results in faster OH consumption. For the OH diffusion timescale, a length scale needs to be chosen and the OH diffusion coefficient is calculated in the present work using a mixture average of the constituent binary diffusion coefficients. The binary diffusion coefficients are calculated via Chapman–Eskog theory (Kee et al., 2003). Importantly, the OH diffusion coefficient scales with $T^{3/2}$. At the flame tip, the major gaseous components are $N_2$, $O_2$, and $CO_2$, and the temperature is in the range 1400–1500 K in the reaction zone where OH and the soot surface is reacting. The reaction zone is roughly 2 mm wide and thus OH has to travel 1 mm to reach of the reaction zone from with side, and thus represents the length scale of diffusion.

$$\tau_D = \frac{L^2}{D(T)} \tag{29}$$

Subsequently, the $\tau_D$ is estimated using average temperature across the reaction zone in Fig. 3. To evaluate an OH consumption timescale an average surface area across the reaction zone is used. The estimated timescales are shown in Table 5, and highlight clearly which fusing models have the ability to burnout and which do not. Fusing, which acts to reduce surface area can influence the burnout behaviour in the non-smoking flame, when fusing is too slow or ignored completely OH is consumed faster then it can diffuse and results in a reduced oxidation rate as seen at r = 2 mm in Fig. 3(d). Importantly, this leads unsuccessful burnout of the remaining soot.

### *7.2. Total number density*

Fig. 4(a) presents the total number density along the path of maximum soot. Both furnace black derived fusing models perform very similarly and slightly underpredict the total number density close to the inlet, then overpredict the falling total number density until HAB 0.04 m. From this point a near-constant value is reached that is broadly consistent with experimental data points. Interestingly, the ethylene-based soot model seems to capture the initially high total number density near the inlet, and shows a steeper decay in total number density as the height above the burner increase. Eventually, the ethylene-based fusing model prediction converges to the predictions obtained with both furnace black fusing models higher up in the flame.

Nucleation and aggregation will dominate the total number density predicted. Nucleation is modelled as a self-dimerisation process, and thus it is not possible to directly associate the different simulated nucleation rates with differing fusing rates. However, via the quadratic dimer balance nucleation and condensation compete for the same precursor. Condensation and aggregation rely on an understanding of the collision diameter of aggregates, which in turn is modelled as a function of aggregate morphology (Eq. (4)). Simply, the more primary particles per aggregate, with the assumed constant fractal dimension of 1.8, the larger its collision diameter and the higher the rate of collision. These collisions can be either dimer-soot or soot–soot. A higher rate of collision between dimers and soot would result in a higher condensation rate, consuming more dimers, and importantly leaving less dimers for nucleation to occur. A higher condensation rate would, via the dimer balance, suppress nucleation. A higher aggregation rate would lead to the total number density reducing more rapidly. Fig. 4(a) alone suggests that aggregation rates were seemingly quenched higher up in the flame across all three fusing models, but that differences in aggregate collision diameter linked to differing fusing rates

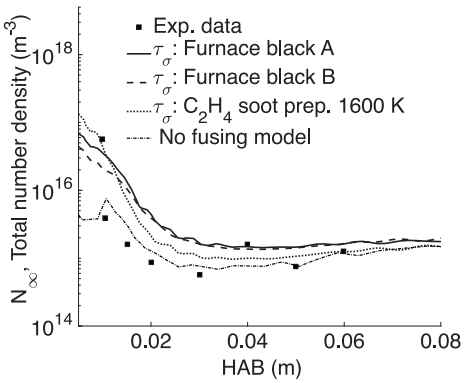


(a) Total number density along the path of maximum soot (Santoro et al., 1987).

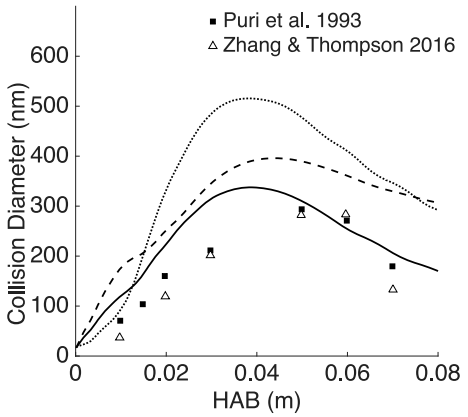


(b) Collision diameters (Puri et al., 1993; Zhang and Thomson, 2016).

**Fig. 4.** Total number density (Santoro et al., 1987) and collision diameters along path of maximum soot (Puri et al., 1993; Zhang & Thomson, 2016).

may be involved close to the inlet. Fig. 4(b) provides some corroborating evidence for this mechanism, namely the ethylene-soot based fusing model predicts the smallest aggregate collision diameter until roughly HAB = 0.015 m consistent with the highest total number density and condensation rate. Shortly afterwards the ethylene-based soot model predicts a rapidly increasing collision diameter, reaching a maximum value of over 500 nm, vastly greater than what is experimentally observed. Furnace black A appears to provide the closest collision diameter prediction particularly higher up in the flame, but number density predictions across the three finite rate model appear similar.

When considering the no-fusing model, the predicted collision diameters were far larger than even the ethylene-based soot models results, ranging in the thousands of nm. This markedly larger collision diameter correspondingly produced the lowest total number close to the inlet. However,after this initial underprediction the no-fusing model seems to capture the experimental data well, in spite of the enormous collision diameters. The inference must be that fusing imparts a meaningful difference on predicting inlet number densities only, and at later stages in the flame fusing plays little to no role in influencing the total number density. However, collision diameter predictions are highly sensitive to aggregate morphology which the chosen fusing mode directly influences.

*7.2.1. Soot morphology*

The three finite rate fusing models display distinctly different trends in the average number of primary particles per aggregate ($N_{av}$) throughout the flame, Fig. 5(a). The furnace black A model seems to overpredict the number of primary particles per aggregate early-on in the flame, with $N_{av}$ predicted to range between 50–80 primary particles per aggregate at around 0.01 m HAB. Beyond 0.03 m HAB, the furnace black A model predicts a number of primary particles per aggregate that is concordant with experimentally observed values, and provides the closest prediction out of all three finite rate fusing models. Furnace black B overpredicts the early value of $N_{av}$ by roughly an order of magnitude, followed by a fall in $N_{av}$ until HAB of roughly 0.03 m. After this point, the furnace black B prediction seems to show an ever-increasing number of primary particles per aggregate that deviates significantly from the experimental data points. The ethylene-soot based fusing model displays a fundamentally different prediction. Early in the flame, the ethylene-soot model predicts the lowest $N_{av}$ of the fusing models, followed by an increasing $N_{av}$ that reaches a gradual maximum at around HAB 0.05 m. With reference to Table 1, clearly the fourth-order dependency on primary particle diameter that the ethylene-soot fusing model employs leads to significantly different evolution of $N_{av}$ compared to the linear primary particle dependence displayed by both furnace black models. The no-fusing model overpredicts $N_{av}$ compared to the experimental data and the three finite rate fusing models, by roughly 3 orders of magnitude, and serves as the extreme limiting case of aggregates that cannot fuse. Clearly, in order to capture the number of primary particles per aggregate fusing must be included.

However, early in flames when surface growth is dominant, there is another mechanism that would act to reduce the number of primary particles per aggregate. Fast surface growth requiring an abundance of acetylene, would increase the diameter of primary particles and necks between primary particles to such an extent, that neighbouring primary particles would eventually be totally encapsulated by this new layer of carbonaceous growth. If this process were fast enough, and crucially faster than the rate of collision between particles, then neighbouring groups of primary particles would be smothered and form a larger, single primary particle. This would reduce the average number of primary particles per aggregate. This process has been called by different names, such as growth-driven restructuring or obliteration. Importantly, growth-driven restructuring does not change the distance between primary particle centres, and can only occur when surface growth is fast, crucially faster that the collision rate. Fast surface growth requires a high acetylene concentration and Fig. 5(a) plots the acetylene mole fraction and number of primary particles per aggregate along the path of maximum soot simultaneously. Growth-driven restructuring is not accounted for in the current work, thus whatever changes in the number of primary particles per aggregate seen in simulation results must be a function of aggregation and the chosen fusing model.

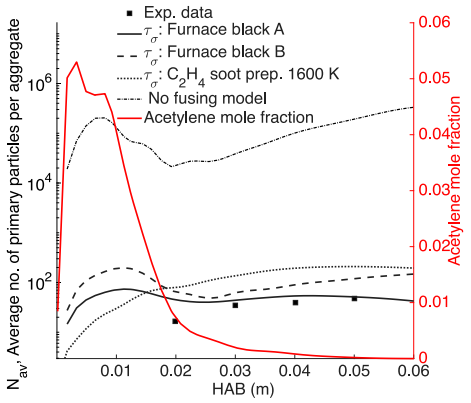


(a) $N_{av}$ (Iyer et al., 2007) and acetylene mole fraction.

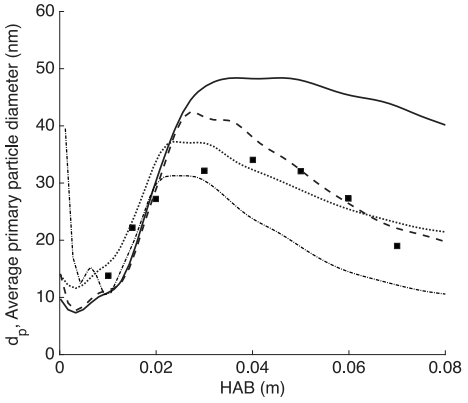


(b) Primary particle diameter (Megaridis Constantine and Dobbins Richard, 1989; Iyer et al., 2007).

**Fig. 5.** Soot morphological features along path of maximum soot in the non-smoking flame (Iyer et al., 2007; Megaridis Constantine & Dobbins Richard, 1989).

The furnace black A model seems to overpredict the level of structure when the acetylene mole fraction is high, and converge to the experimentally observed values when the acetylene is rapidly consumed higher up in the flame (HAB = 0.03 m and above). Furnace black B produces a similar pattern early on but deviates higher up in the flame despite the decreasing acetylene mole fraction. The ethylene-soot based fusing model appears to produce low levels of $N_{av}$ in the high acetylene region, and then overpredict the level of $N_{av}$ higher up in the flame where surface growth reduces. Without explicitly accounting for the effect of growth-driven restructuring it is hard to apportion the contributions of each restructuring mechanism when the acetylene mole fraction is high. However, it appears that the fourth order primary particle dependence associated with the ethylene-soot fusing model mimics the early low level of primary particles per aggregate that could plausibly be attributed to growth-driven restructuring in the high acetylene region.

The linear primary particle models derived from furnace black suggest a clear distinction between the two restructuring regimes, and are unable to predict a low level of primary particles per aggregate in the high acetylene regime. It is suggested that perhaps the fourth order fusing law associated with the ethylene-based fusing model is inadvertently accounting for both forms of restructuring at the expense of capturing either phenomenon correctly. On the other hand, the linear fusing laws, and in particular furnace black A which is derived from the more oxygenated group of furnace black proxies, seems to capture fusing alone correctly, whilst justifiably not accounting for growth-driven restructuring at all. Clearly fusing plays a pivotal role in predicting the average number of primary particle per aggregate in the absence of high acetylene concentrations.

Next, Fig. 5(b) presents the average primary particle diameter along the path of maximum soot. In the early stages of the flame the three carbonaceous-based fusing models perform similarly, and the primary particle size rises. However, each carbonaceous-based model predicts a different peak primary particle size at subsequently greater heights above the burner. First, the ethylene-soot based model predicts a peak size of roughly 38 nm at 0.02 HAB. Second, the furnace black B fusing model predicts a peak primary particle size of roughly 40 nm, at a later HAB of approximately 0.03 m, whilst the furnace black A model predicts a peak primary particle size close to 50 nm at roughly 0.035 m HAB. It appears that the furnace black A model most closely predicts the average number of primary particles per aggregate, but with a primary particle diameter that is 10–20 nm too large. Whilst the furnace black B and ethylene-soot based fusing models, significantly overpredicted the number of primary particles per aggregates, whilst more closely capturing their size relative to experimental values.

Fusing can only act to increase the primary particle diameter, whilst surface reactions can act either increase or decrease primary particle size depending on whether growth or oxidation is dominant. The no-fusing model provides evidence as to how the average primary particles size evolves due to growth and oxidation alone and serves as a conceptual baseline. At inlet, the no-fusing model predicts large primary particles (40 nm) that corresponds with the enormous growth seen in Fig. 1(a). Next, the no-fusing model predictions closely follows the other results until HAB = 0.025 m. Beyond this, the no-fusing model significantly underpredicts the primary particle size.

The balance of fusing and oxidation will determine the eventual primary particle size, and since Fig. 5(a) suggests that the level of $N_{av}$ was correctly accounted for using the furnace black A model, perhaps the rate of oxidation along the pathline of maximum soot is under-estimated. Clearly, some aspects of soot morphology can be directly attributed to the fusing model used, whilst others such as the primary particle diameter predictions have to be considered in conjunction with soot surface reactions and their own associated uncertainties.

### *7.3. Incipient smoking flame*

Fig. 6(a) shows the predicted integrated soot volume fraction in the incipient smoking case. As the name suggests, a small yet visible quantity of soot should be emitted from the flame. In order to highlight this, Fig. 6(b) shows an enlarged view of the exit

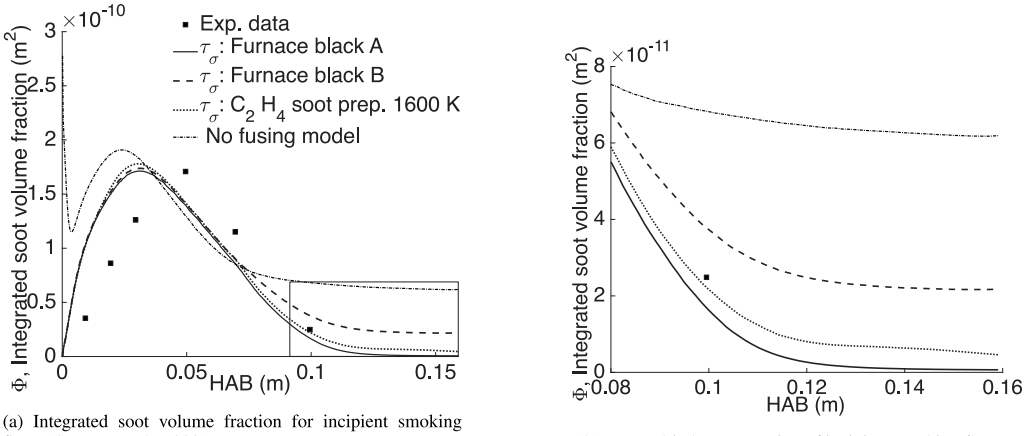


(a) Integrated soot volume fraction for incipient smoking flame (Santoro et al., 1983).

(b) Zoomed-in burnout region of incipient smoking flame.

**Fig. 6.** Soot volume fraction throughout incipient smoking flame.

region of the flame. All three carbonaceous-based fusing models produced qualitatively the same correct behaviour when considering the non-zero quantity of soot emitted. Furthermore, the no no-fusing model has been included and predicts similar non-zero levels of soot being emitted from the flame as well as the burst of soot generation close to the inlet. The furnace black B model predicted a far larger quantity of soot being emitted compared to the other fusing models, whereas furnace black A produced the smallest quantity. Furnace black A produced a small value of integrated volume fraction seen at exit, which corresponds to a local soot volume fraction of approximately 0.1 ppm. The ethylene-soot based model produced more soot, and an exit local volume fraction that corresponds to roughly 0.2 ppm. Moreover, this quantity of soot extend over a larger area when compared to the results from the simulation using the furnace black A model. Further experimental datasets regarding the incipient smoking case, to the authors' knowledge, do not exist. However, the furnace black A and ethylene-based soot fusing models correctly predicted the qualitative results of an incipient smoking flame, whilst the furnace black B model appears to predict a larger quantity of soot being emitted. Essentially, this qualitatively confirms the overall burnout characteristics in the simulated incipient flames. Furthermore, this implies the balance between surface area minimisation due to fusing and oxidation rates has been captured correctly. The fact that the no-fusing model fails to predict this basic feature shows that simply ignoring fusing does negatively affect burnout behaviour as seen in the non-smoking flame

### *7.4. Smoking flame*

Similar to the incipient smoking case, the smoking flame is relatively less well documented than the non-smoking case. Clear, visible smoke should be emitted as the soot generated fails to burnout completely. The furnace black A model seems to predict a flame that almost burns out entirely in a manner similar to the incipient smoking case (Fig. 7). Although a small, non-zero quantity of soot is seen at exit, this is a vast underprediction compared to experimental data points close to the exit. Conversely, the furnace black B model closely predicts the quantity of soot emitted at exit as well as matching the peak integrated soot volume fraction value seen experimentally, albeit at a lower HAB. Finally, the ethylene-soot fusing model derived from a soot sample generated at a pyrolisis temperature of 1800 K, as opposed 1600 K was implemented. The higher pyrolysis temperature, corresponds to a greater quantity of acetylene being produced during particle formation, and more closely matches the higher acetylene environment that the relatively fuel-rich smoking flame produces. The ethylene-soot sample closely predicted the quantity of soot emitted at exit, although in this case overpredicted the integrated soot volume fraction.

Interestingly, the no-fusing model predicts a level of soot beyond HAB = 0.1 broadly consistent with the smoking nature of this flame. Although the no-fusing model overpredicts the total quantity of soot high up in the smoking flame, when compared to the incipient and non-smoking cases, this is the best agreement with experimental observations and perhaps in order to capture the smoking nature of this flame fusing plays a less important role than in the burnout region in the incipient and non-smoking flames.

Fig. 8(b) shows the evolution of the average primary particle diameter along the pathline of maximum soot. All three carbonaceous-based fusing models show meaningfully different behaviour. The furnace black A model significantly overpredicts the primary particle size for the majority of the path. Only in the very early stages of the flame, below HAB 0.02 m does the furnace black A model predict primary particles size similar to the other two carbonaceous-based fusing models and experimental data points. The ethylene-soot based model (prepared at 1800 K) appears to underpredict the primary particle size throughout the flame, and show a peak primary particle size at a lower HAB than observed experimentally. The furnace black B model best predicts the primary particle size higher up in the flame when oxidation is dominant. The peak primary size predicted by the furnace black B model is higher than the experimentally seen value but lower than the furnace black A prediction. Without an accompanying set of experimental results describing the average number of primary particles per aggregate, it is difficult to quantitatively assess each fusing model and its ability to predict soot morphology in the smoking flame case. As can be seen in the non-smoking case, even if

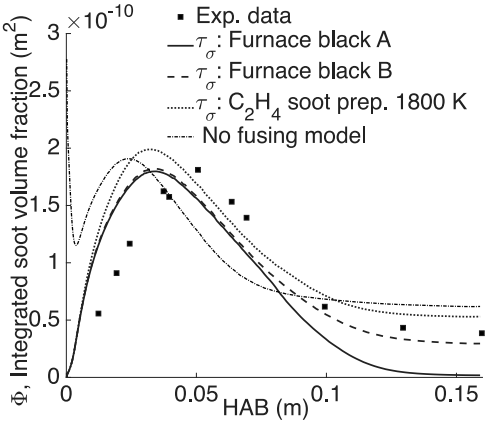


**Fig. 7.** Integrated soot volume fraction for smoking flame (Santoro et al., 1983).

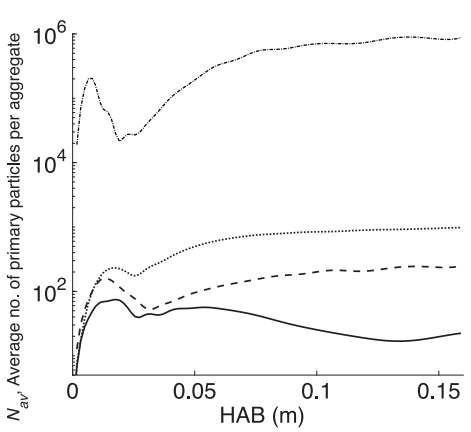


(a) $N_{av}$ along ath of maximum soot in the smoking flame.

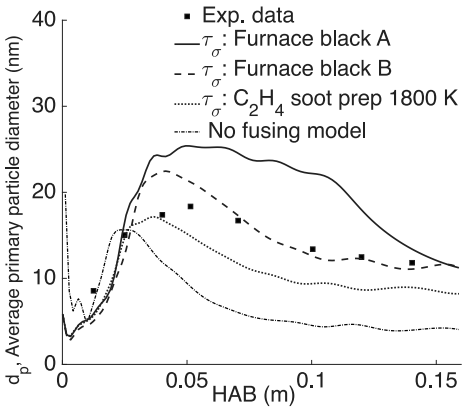


(b) Primary particle diameter along path of maximum soot in the smoking flame (Santoro et al., 1983).

**Fig. 8.** Morphological features of soot aggregates along path of maximum soot in the smoking flame.

the number of primary particles per aggregate is predicted correctly, this does not guarantee that the size of said primary particles will also align closely with experimental data. The furnace black B model most faithfully recreates the average primary particle size in the smoking flame despite overpredicting the peak primary particle size by roughly 10 nm. The no-fusing model again serves as the conceptual baseline when considering the average primary particle diameter. Only growth and oxidation can alter the primary particle size in the no-fusing results, and clearly without fusing the primary particle diameter in underpredicted beyond HAB = 0.05 m. The no-fusing model again displays the initial large primary particle sizes with an intermediate region where predictions align with the other fusing models (HAB 0.01–0.025 m). However, the no-fusing model provides the worst prediction of primary particle diameter and fusing clearly plays a role in determining the primary particle size in the smoking flame, with the higher activation temperature furnace black B model providing the best predictions.

To the authors' knowledge, no quantitative measurement of the average number of primary particles per aggregate exists for the smoking flame case. Thus, predictions corresponding to each fusing model can only be contrasted amongst themselves, without reference to experimental observations. Fig. 8(a) presents the average number of primary particles per aggregate along the path of maximum soot in the smoking flame. At exit (HAB = 0.16 m) there is a striking difference in the level of $N_{av}$ predicted across the all fusing models. The ethylene-soot fusing model predicts $\approx$ 1000 primary particles per aggregate, whereas the furnace black A model predicts roughly 20. Furnace black A overpredicts the primary particle diameter throughout the smoking flame (Fig. 8(b)). Since aggregate fusing causes an increase in primary particle diameter at the cost of reducing the number of primary particles, it is reasonable to expect the furnace black A model to predict a significantly reduced number of primary particles per aggregate. Conversely, the ethylene-based based model predicted the relatively small primary particle diameters high up in the flame, and this is indicative of a slower rate of fusing. Slower fusing corresponds a far higher number of primary particles per aggregate, and the ethylene-based model exhibits this trend. Finally, the furnace black B model appears to show a rate of fusing that is somewhere in between the two other fusing models. Fig. 8(a) shows that the level of $N_{av}$ predicted in the smoking flame is highly sensitive to the fusing model used, and even though the furnace black B and ethylene-based fusing models produced similar integrated soot

volume fraction predictions, there is a significant difference in the predicted number of primary particles per aggregate. Finally, the no-fusing model again vastly overpredicts the level of $N_{av}$ by at least 3 orders of magnitude and shows some level of fusing is required to produce plausible levels of $N_{av}$ in the smoking case.

### 7.5. Further analysis of burnout and fusing

More generally, the integrated soot volume fraction results across all three Santoro flames reveal the role the fusing timescale plays alongside oxidation in order to correctly predict the burnout behaviour. These qualitative results are summarised in Table 6, where a tick represents that the quantity of soot emitted from the flame was considered consistent with the description of the flame as non-smoking, incipient smoking, or smoking. Notably, the lower activation temperature fusing models (furnace black A and ethylene-soot prep. 1600 K) appear to capture the burnout behaviour of non-smoking and incipient smoking flame whilst struggle to predict the greater quantity of soot emitted in the smoking flame case. Conversely, the higher activation temperature models seem to correctly capture the smoking flame.

**Table 6**
Flame burnout results.

| | Furnace black A $T_a$ = 5,199 K | Furnace black B $T_a$ = 15,617 K | Ethylene-soot prep. 1600 K $T_a$ = 12,066 K | Ethylene-soot prep. 1800 K $T_a$ = 16,812 K |
|---|---|---|---|---|
| Non-smoking (NS) | ✓ | X | ✓ | – |
| Incipient Smoking (IS) | ✓ | X | ✓ | – |
| Smoking (S) | X | ✓ | – | ✓ |

Fusing rates are intrinsically linked to the material properties of the aggregates in question. In Section 2 the activation temperatures presented for each fusing law in simple terms capture how easily the underlying material fuses. The lower the fusing activation temperature, the more easily a material fuses. The key difference in each variant of Santoro flame experiment is the fuel flow rate and Santoro et al. (1987) concludes that the *'increase in the amount of soot formed in these flames is primarily due to the increase in the residence time in the annular region in the flame'* when contrasting the non-smoking and smoking flames. Potentially, the difference in the residence time throughout the soot formation region in each flame leads to differences in the composition of the soot aggregates that assemble. With higher fuel flow rates and longer formation residence times, the higher activation temperature fusing models appear more appropriate.

A more quantitative approach would be to use the insight from Kholghy et al. (2016) and consider the H/C ratio of soot. There is an approximate exponential relationship that links the H/C ratio of PAH compounds to the approximate molecular weight. A characteristic PAH involved in nucleation and condensation such as pyrene ($C_{16}H_{10}$) has a H/C ratio of 0.625. Nascent soot is modelled to be made up of PAH molecules similar to pyrene with H/C ratios of around 0.6. Highly hydrogenated soot such as this has no internal order and PAH molecules are arranged randomly within the soot particle (Kholghy et al., 2016). This exposes reactive edges at the soot surface that are modelled via the HACA approach, to then react with acetylene and add mass. On average, the HACA mechanisms adds 1 H atom for every 4 C atoms added (H/C = 0.25) (Kholghy et al., 2016; Whitesides et al., 2009, 2007). On the contrary, when the H/C ratio is low (H/C ≈ 0.3), the soot is said to be graphitised with a hard shell, where the PAH molecules within soot particles are oriented with a *face-on-surface* structure (Kholghy et al., 2016). However, the condensation of gaseous PAHs onto existing soot particles must add mass at the H/C of the gaseous PAH itself, roughly 0.6. Thus, considering rates of mass addition via condensation and surface growth (HACA), the weighted H/C of new mass added to a nascent soot particle can be described as follows:

$$\left(\frac{H}{C}\right)_{in} = \frac{W\left(\frac{H}{C}\right)_{PAH} + \left(\frac{H}{C}\right)_{HACA}}{1+W} \tag{30}$$

where

$$W = \frac{\dot{\Omega}_{cond}}{\dot{\Omega}_{HACA}} \tag{31}$$

Here, $\dot{\Omega}_{cond}$ represents the soot volume fraction addition rate per second due to condensation and is essentially the integral of the RHS of Eq. (19). Similarly, $\dot{\Omega}_{HACA}$ can be constructed by taking the first moment of RHS of Eq. (8). By assuming that $W$ and $(H/C)_{in}$ remain constant as a soot particle grows in mass, a simplified evolution equation for (H/C)(t) can be derived and some illustrative asymptotic cases identified (see the full derivation in Appendix C):

$$\frac{H}{C}(t) = \left(\frac{H}{C}\right)_{in} - \frac{\left(\frac{H}{C}\right)_{in} - \frac{H}{C}(0)}{\frac{m(t)}{m(0)}} \tag{32}$$

Note that the soot particle composition is not computed explicitly in the present work, and Eq. (32) is a simplified representation. When $W \gg 1$, (H/C)(t) remains effectively pinned at the higher $(H/C)_{in}$ of 0.6. With pure HACA mass addition ($W = 0$, $(H/C)_{in}$ =

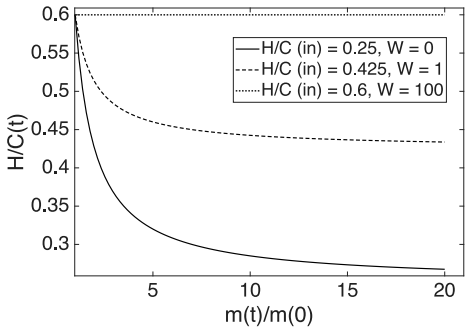


(a) $N_{av}$ along path of maximum soot in the smoking flame.

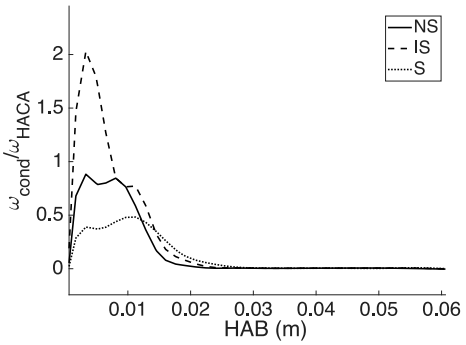


(b) Primary particle diameter along path of maximum soot in the smoking flame (Santoro et al., 1983).

**Fig. 9.** Morphological features of soot aggregates along path of maximum soot in the smoking flame.

0.25), the (H/C)(t) drops rapidly and, when the normalised mass reaches 5, the H/C reaches 0.3, which corresponds to a graphitic type of soot.

Considering these effects in the Santoro flames along the path of maximum soot, Fig. 9(b) shows that the NS flame and IS flame have early regions where the condensation rate is of the same order as the HACA mass addition rate. Thus we expect the H/C ratio of NS and IS flames to be maintained at the higher end of the H/C spectrum, close to 0.6 in this early region, and the soot is expected to fuse more easily. However, the S flame has a noticeably lower condensation rate relative to the surface growth (HACA) rate, and instead we can deduce that the soot present in the S flame is becoming more graphitic more quickly than the other two flames, thus warranting the furnace black B fusing model.

It can also be seen that, after about 0.2 m (HAB), all three flames become HACA-dominated, and the H/C ratio must begin to drop rapidly. As alluded to, perhaps as little as 5 mass generations or an increase in $5^{1/3} \approx 1.7$ in diameter is indicative of the soot becoming fully graphitized once HACA becomes dominant.

Furthermore, this behaviour seems to be related to the smoke point. Below and up to the smoke point (incipient smoking flame), condensation appears to be significant enough to delay the onset of the rapid drop in H/C ratio early in the flame, and thus warrants a fusing model with a lower activation temperature. However, when the flame becomes fully smoking, the HACA mechanism becomes dominant throughout and the H/C ratio likely drops far sooner in the flame warranting the higher activation temperature in the fusing model, i.e. furnace black B.

It should be noted that this is a simplified order-of-magnitude analysis, since the present simulations do not include computation of the H/C ratio. To extend this argument to other cases, knowledge of the production of PAHs relative to acetylene is needed, as well as estimation of the subsequent mass addition rates. This can in turn be interpreted as H/C addition at certain limiting cases.

## 8. Conclusions

The two-PBE methodology (Sun et al., 2021) has been successfully used to simulate all three variants of the Santoro flame experiments: non-smoking, incipient smoking, and smoking. Importantly, the two-PBE approach allowed for the effects of aggregate fusing to be included, and accordingly a set of carbonaceous-based fusing timescale models were implemented. Namely: the two previously validated furnace black (A&B) based models of O'Sullivan et al. (2025) as well as ethylene-soot based fusing model of Matsukawa et al. (2023).

Considering the integrated soot volume fraction, two distinct types of burnout behaviour were predicted. The lower activation temperature furnace black model A and the ethylene-soot model correctly predicted the total burnout of the flame, whilst the higher activation energy furnace black B model predicted soot escaping the flame as smoke. The timescale for OH consumption due to reaction with soot was found to vary with the inverse of soot surface area and, when considered against the timescale for OH diffusion, it was found that the furnace black B simulation produced localised OH starvation at the flame tip. Soot aggregate fusing and its direct influence on surface area was found to be linked with burnout behaviour among the flame simulations

Regarding the path of maximum soot, the furnace black A model correctly predicted the average number of primary particle per aggregate in the non-smoking flame at heights of 0.03 m and above, but significantly overpredicted the average primary particle diameter in the same region. The furnace black B and ethylene fusing models significantly overpredicted the number of primary particles per aggregate, but produced more realistic primary particle size predictions. These results elucidate the role of fusing in the evolution of soot aggregate morphology.

Considering the incipient smoking flame, the furnace black A and ethylene-soot based models produced qualitatively the correct burnout behaviour, with only a small quantity of soot escaping the flame. The furnace black B model predicted a far higher quantity of soot emitted as smoke.

The higher activation temperature furnace black B model and the ethylene-soot fusing model (prepared at 1800 K) both captured the integrated soot volume fraction at exit in the smoking flame. Conversely, the lower activation temperature furnace black A model

predicted near total burnout, in stark contrast to the experimental observations. The furnace black B model captured the evolution of primary particle size along the path of maximum soot very closely when compared to experimental data.

To conclude, the furnace black A and ethylene-soot (prepared at 1600 K) fusing models performed best in the non-smoking and incipient smoking flames. The furnace black A model captured the average number of primary particles per aggregate and collision diameter of aggregates more closely than the ethylene-soot (prep. 1600 K) fusing model, whilst the latter better predicted the average primary particle size in the non-smoking flame. The higher activation temperature furnace black B performed best in the smoking flame case. These results highlight the role of soot composition in the choice of fusing model.

## CRediT authorship contribution statement

**Daniel O'Sullivan:** Writing – original draft, Visualization, Validation, Software, Methodology, Investigation, Formal analysis, Data curation, Conceptualization. **Stelios Rigopoulos:** Writing – review & editing, Supervision, Software, Resources, Project administration, Methodology, Investigation, Funding acquisition, Conceptualization.

## Declaration of competing interest

The authors declare that they have no known competing financial interests or personal relationships that could have appeared to influence the work reported in this paper.

## Acknowledgements

Daniel O'Sullivan gratefully acknowledges the financial support by the Engineering and Physical Sciences Research Council (EPSRC), United Kingdom in the form of a Doctoral Training Partnership (DTP) [grant number EP/R513052/1]. The authors also wish to acknowledge the Imperial College Research Computing Service (https://doi.org/10.14469/hpc/2232) for providing computational resources, and finally Russel B. Diemer Jr. for insightful discussions.

## Appendix A. Radial profiles

Figs. A.10 and A.11 show the radial temperature profiles at selected HABs low down or high up in the flame respectively. Across all four HABs, there is close agreement with experimental data points. Where results are near identical only a single curve is shown. This is the case for all models in Fig. A.10.

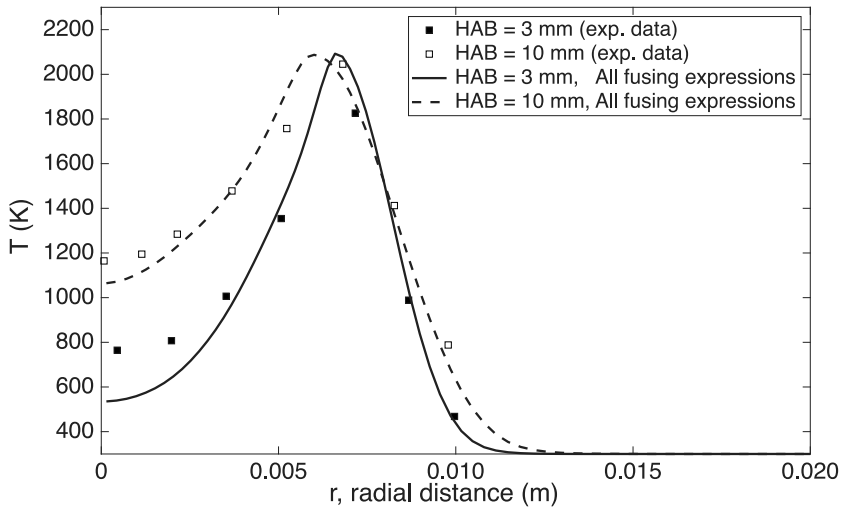


**Fig. A.10.** Temperature distribution along radial direction at early heights above the burner (Santoro et al., 1987). All fusing models (Table 1) produced identical temperature distributions.

Fig. A.12 shows the radial distribution of OH radicals at two HABs. Laser-induced fluorescence (LIF) was used to measure the OH radical mole fraction and experimental uncertainty has been known to be as high as 50% (Kennedy et al., 1996). In light of the large experimental uncertainty, this agreement of OH radial distributions can be viewed as reasonable, with the underprediction in OH close to the centreline linked to surface area predictions of aggregates.

Fig. A.13 presents radial distributions of the acetylene mole fraction at HAB of 7 mm and 20 mm. Acetylene plays a pivotal role in the surface growth of soot particles, and is most important at low heights above the burner where nucleation and growth are

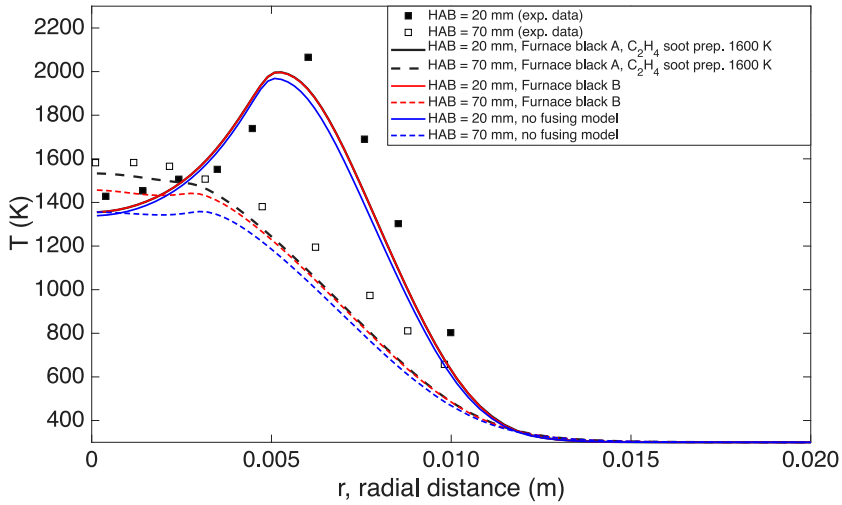


**Fig. A.11.** Temperature distribution along radial direction at later heights above the burner (Santoro et al., 1987). All fusing models (Table 1) produced identical temperature distributions.

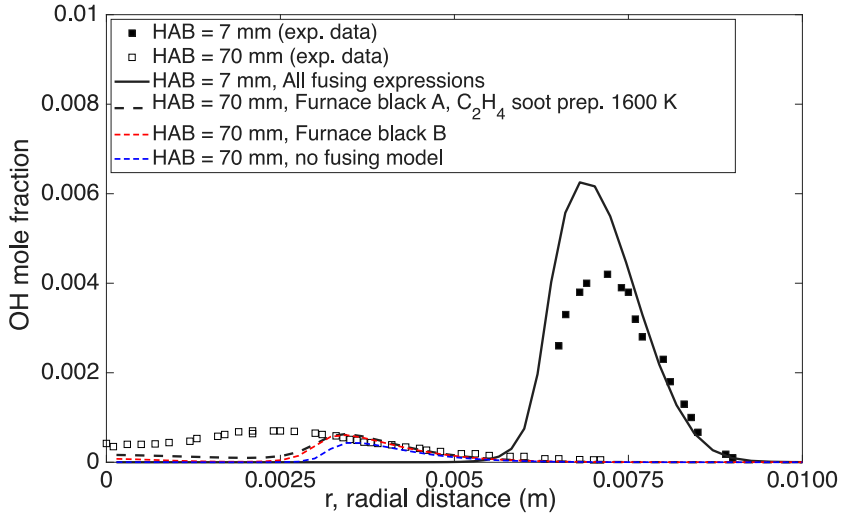


**Fig. A.12.** OH mole fraction radial distributions (Santoro et al., 1987).

most prominent. At 7 mm HAB, all three fusing models predicted an identical radial distribution that overpredicts the measured acetylene mole fraction, although the shape of the curve appears concordant and correctly centred with respect to the experimental data points. Higher up in the flame at 20 mm, the predicted acetylene radial distribution closely aligns with observed experimental values, and once again all three fusing models generated identical radial distributions. Notably, other researchers have observed similar results in simulation predictions of radial acetylene distributions (Akridis & Rigopoulos, 2017; Veshkini et al., 2016; Zhang et al., 2009) and this is likely due to the uncertainty surrounding the degree of fuel preheating at inlet.

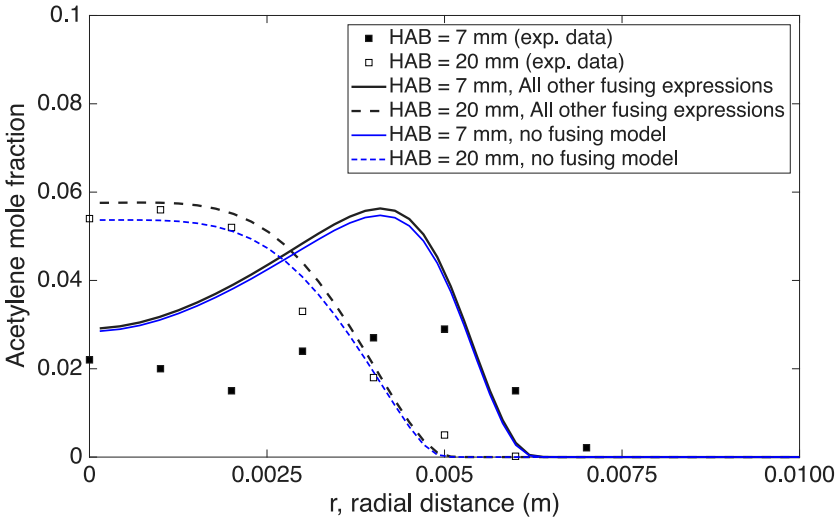


**Fig. A.13.** Acetylene mole fraction radial distributions (Kennedy et al., 1996).

## Appendix B. Centreline PAH and total number density profiles

See Fig. B.14

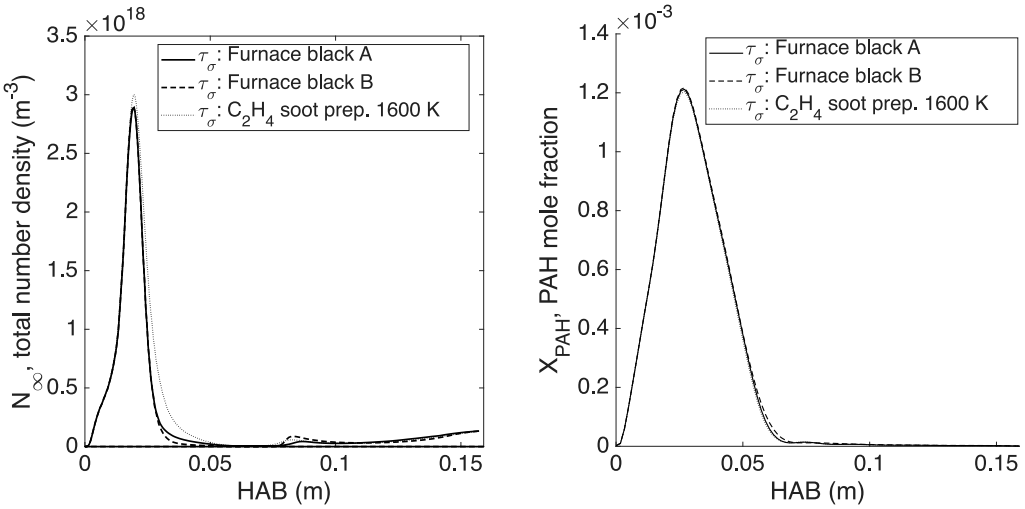


(a) Total number density along centreline in the non-smoking flame, showing little variation among the three finite-rate fusing models.

(b) Combined mole fraction of major PAHs involved in nucleation and condensation and benzene, showing little variation among the three fusing models.

**Fig. B.14.** Centreline profiles of species involved in nucleation and condensation in the non-smoking flame.

## Appendix C. H/C ratio evolution under simplified conditions

Consider a single soot particle with initial mass $m(t)$ and initial H/C ratio $H/C(t)$ of soot particle. Across $\delta t$, a small amount of new mass is added, $\delta m$, with a constant incident H/C ratio - $(H/C)_{in}$. Thus the mass-weighted H/C ratio at time $t + \delta t$ is:

$$\frac{H}{C}(t+\delta t) = \frac{m(t)}{m(t+\delta t)} \quad \frac{H}{C}(t) + \frac{\delta m}{m(t+\delta t)} \left(\frac{H}{C}\right)_{in} \tag{C.1}$$

Using a first order Taylor approximation for $m(t+\delta t) = m(t) + \frac{dm}{dt}\delta t + \mathcal{O}(\delta t^2)$ and the change in H/C ratio, we obtain:

$$\frac{H}{C}(t+\delta t) - \frac{H}{C}(t) = \left[ \frac{\cancel{m(t)} - \cancel{m(t)} - \frac{dm}{dt}\delta t}{m(t) + \frac{dm}{dt}\delta t)} \right] \frac{H}{C}(t) + \frac{\frac{dm}{dt}\delta t}{m(t) + \frac{dm}{dt}\delta t} \left(\frac{H}{C}\right)_{in} \tag{C.2}$$

Divide throughout by $\delta t$ and then taking limits $\delta t \to 0$:

$$\frac{d\frac{H}{C}(t)}{dt} = \frac{\frac{dm}{dt}}{m(t)} \left[ \left(\frac{H}{C}\right)_{in} - \frac{H}{C}(t) \right] \tag{C.3}$$

which admits the solution:

$$\frac{H}{C}(t) = \left(\frac{H}{C}\right)_{in} - \frac{\left(\left(\frac{H}{C}\right)_{in} - \frac{H}{C}(0)\right)}{\frac{m(t)}{m(0)}} \tag{C.4}$$

## Appendix D. Supplementary data

Supplementary material includes particle size distributions $n(v)$ and $n_p(v)$ for each of the three flames at various points along the path of maximum soot. Unfortunately, to the Authors' knowledge no experimental data exists to directly compare the particle size distributions, but comparison between each fusing model and its effect on the distributions can be seen.

Supplementary material related to this article can be found online at https://doi.org/10.1016/j.jaerosci.2026.106758.

## Data availability

Data will be made available on request.

## References


Akridis, P., & Rigopoulos, S. (2017). Modelling of soot formation in laminar diffusion flames using a comprehensive CFD-PBE model with detailed gas-phase chemistry. *Combustion Theory and Modelling*, *21*(1), 35–48.

Blanquart, G., Pepiot-Desjardins, P., & Pitsch, H. (2009). Chemical mechanism for high temperature combustion of engine relevant fuels with emphasis on soot precursors. *Combustion and Flame*, *156*(3), 588–607.

Blanquart, G., & Pitsch, H. (2009). A joint volume-surface-hydrogen multi-variate model for soot formation. In H. Bockhorn, A. D'Anna, A. F. Sarofin, & H. Wang (Eds.), *Combustion generated fine carbonaceous particles* (pp. 437–463). KIT scientific publishing.

Blanquart, G., & Pitsch, H. (2009). Analyzing the effects of temperature on soot formation with a joint volume-surface-hydrogen model. *Combustion and Flame*, *156*, 1614–1626.

Bond, T. C., Doherty, S. J., Fahey, D. W., Forster, P. M., Berntsen, T., Deangelo, B. J., Flanner, M. G., Ghan, S., Kärcher, B., Koch, D., Kinne, S., Kondo, Y., Quinn, P. K., Sarofim, M. C., Schultz, M. G., Schulz, M., Venkataraman, C., Zhang, H., Zhang, S., .... Zender, C. S. (2013). Bounding the role of black carbon in the climate system: A scientific assessment. *Journal of Geophysical Research: Atmospheres*, *118*(11), 5380–5552.

Brasil, A. M., Farias, T. L., & Carvalho, M. G. (1999). A recipe for image characterization of fractal-like aggregates. *Journal of Aerosol Science*, *30*(10), 1379–1389.

Chen, D., Zainuddin, Z., Yapp, E., Akroyd, J., Mosbach, S., & Kraft, M. (2013). A fully coupled simulation of PAH and soot growth with a population balance model. *Proceedings of the Combustion Institute*, *34*(1), 1827–1835.

Diemer, R. B. (2023). Simplifying population balance models to promote broader use in industry. *Chemical Engineering Research and Design*, *190*, 91–105.

Dworkin, S. B., Zhang, Q., Thomson, M. J., Slavinskaya, N. A., & Riedel, U. (2011). Application of an enhanced PAH growth model to soot formation in a laminar coflow ethylene/air diffusion flame. *Combustion and Flame*, *158*(9), 1682–1695.

Forestieri, S. D., Helgestad, T. M., Lambe, A. T., Renbaum-Wolff, L., Lack, D. A., Massoli, P., Cross, E. S., Dubey, M. K., Mazzoleni, C., Olfert, J. S., Sedlacek, A. J., Freedman, A., Davidovits, P., Onasch, T. B., & Cappa, C. D. (2018). Measurement and modeling of the multiwavelength optical properties of uncoated flame-generated soot. *Atmospheric Chemistry and Physics*, *18*(16), 12141–12159.

Frenklach, M., & Wang, H. (1991). Detailed modeling of soot particle nucleation and growth. *Symposium (International) on Combustion*, *23*(1), 1559–1566.

Friedlander, S. K. (2000). *Smoke, dust, and haze: Fundamentals of aerosol dynamics* (2nd ed.). Oxford University Press.

Friedlander, S. K., & Wu, M. K. (1994). Linear rate law for the decay of the excess surface area of a coalescing solid particle. *Physical Review B*, *49*(5), 3622.

Guo, H., Liu, F., Smallwood, G. J., & Gülder, Ö. L. (2002). The flame preheating effect on numerical modelling of soot formation in a two-dimensional laminar ethylene-air diffusion flame. *Combustion Theory and Modelling*, *6*(2), 173.

Guo, H., Liu, F., Smallwood, G. J., & Gülder, Ö. L. (2006). Numerical study on the influence of hydrogen addition on soot formation in a laminar ethylene–air diffusion flame. *Combustion and Flame*, *145*(1–2), 324–338.

Gwaze, P., Schmid, O., Annegarn, H. J., Andreae, M. O., Huth, J., & Helas, G. (2006). Comparison of three methods of fractal analysis applied to soot aggregates from wood combustion. *Journal of Aerosol Science*, *37*(7), 820–838.

Hairer, E., Norsett, S. P., & Wanner, G. (1993). *Solving ordinary differential equations I. Nonstiff problems* (2nd ed.). Springer-Verlag.

Harding, L. B., Georgievskii, Y., & Klippenstein, S. J. (2005). Predictive theory for hydrogen atom-hydrocarbon radical association kinetics. *Journal of Physical Chemistry A*, *109*(21), 4646–4656.

Harris, S. J., & Kennedy, I. M. (1988). The coagulation of soot particles with van der Waals forces. *Combustion Science and Technology*, *59*(4–6), 443–454.

Iyer, S. S., Litzinger, T. A., Lee, S. Y., & Santoro, R. J. (2007). Determination of soot scattering coefficient from extinction and three-angle scattering in a laminar diffusion flame. *Combustion and Flame*, *149*(1–2), 206–216.
Jones, W. P., di Mare, F., & Marquis, A. J. (2002). *LES-BOFFIN: User's guide: Technical report*, London: Imperial College London.
Karsch, M., & Kronenburg, A. (2023). Modelling nanoparticle agglomeration in the transition regime: A comparison between detailed Langevin Dynamics and population balance calculations. *Journal of Aerosol Science*, *173*, Article 106228.
Karsch, M., Kronenburg, A., & Stein, O. T. (2022). Coagulation rate coefficients for fractal-like agglomerates in the diffusive and ballistic limits. *Chemical Engineering Research and Design*, *187*, 611–622.
Kazakov, A., & Frenklach, M. (1998). Dynamic modeling of soot particle coagulation and aggregation: Implementation with the method of moments and application to high-pressure laminar premixed flames. *Combustion and Flame*, *114*(4), 484–501.
Kazakov, A., Wang, H., & Frenklach, M. (1995). Detailed modeling of soot formation in laminar premixed ethylene flames at a pressure of 10 bar. *Combustion and Flame*, *100*(1–2), 111–120.
Kee, R. J., Coltrin, M. E., & Glarborg, P. (2003). *Chemically reacting flow: Theory and practice* (1st ed.). Wiley.
Kelesidis, G. A., Goudeli, E., & Pratsinis, S. E. (2017). Flame synthesis of functional nanostructured materials and devices: Surface growth and aggregation. *Proceedings of the Combustion Institute*, *36*(1), 29–50.
Kelesidis, G. A., & Pratsinis, S. E. (2022). Santoro flame: The volume fraction of soot accounting for its morphology & composition. *Combustion and Flame*, *240*, Article 112025.
Kennedy, I. M., Yam, C., Rapp, D. C., & Santoro, R. J. (1996). Modeling and measurements of soot and species in a laminar diffusion flame. *Combustion and Flame*, *107*(4), 368–382.
Kholghy, M. R., Veshkini, A., & Thomson, M. J. (2016). The core-shell internal nanostructure of soot - A criterion to model soot maturity. *Carbon*, *100*, 508–536.
Koch, W., & Friedlander, S. K. (1989). The effect of particle coalescence on the surface area of a coagulating aerosol. *Journal of Aerosol Science*, *20*(8), 891–894.
Köylü, Ü. Ö., Faeth, G. M., Farias, T. L., & Carvalho, M. G. (1995). Fractal and projected structure properties of soot aggregates. *Combustion and Flame*, *100*(4), 621–633.
Köylü, Ü. Ö., Mcenally, C. S., Rosner, D. E., & Pfefferle, L. D. (1997). Simultaneous measurements of soot volume fraction and particle size / microstructure in flames using a thermophoretic sampling technique. *Combustion and Flame*, *110*(4), 494–507.
Kruis, F., Kusters, K. A., Pratsinis, S. E., & Scarlett, B. (1993). A simple model for the evolution of the characteristics of aggregate particles undergoing coagulation and sintering. *Aerosol Science and Technology*, *19*(4), 514–526.
Li, X., He, F., Hu, S., Sun, N., Huo, C., & Liu, R. (2023). The culprits of superoxide dismutase inactivation under size-dependent stress of ultrafine carbon black: Superoxide anion, genotoxicity and protein corona. *Science of the Total Environment*, *862*, Article 160770.
Link, O., Snelling, D. R., Thomson, K. A., & Smallwood, G. J. (2011). Development of absolute intensity multi-angle light scattering for the determination of polydisperse soot aggregate properties. *Proceedings of the Combustion Institute*, *33*(1), 847–854.
Liu, A., Garcia, C. E., Sewerin, F., Williams, B. A., & Rigopoulos, S. (2020). Population balance modelling and laser diagnostic validation of soot particle evolution in laminar ethylene diffusion flames. *Combustion and Flame*, *221*, 384–400.
Liu, L., & Mishchenko, M. I. (2018). Scattering and radiative properties of morphologically complex carbonaceous aerosols: A systematic modeling study. *Remote Sensing*, *10*(10), 1634.
Liu, A., & Rigopoulos, S. (2019). A conservative method for numerical solution of the population balance equation, and application to soot formation. *Combustion and Flame*, *205*, 506–521.
Marchal, C. (2008). *Modelisation de la Formation et L'Oxydation des Suies Dans Un Motor Automotive* (Ph.D. thesis), Université d'Orléans.
Maricq, M. M. (2007). Coagulation dynamics of fractal-like soot aggregates. *Journal of Aerosol Science*, *38*(2), 141–156.
Matsukawa, Y., Dewa, K., Era, K., Aoki, T., & Aoki, H. (2023). Experimental coalescence characteristic time of carbon nanoparticle produced from ethylene or benzene pyrolysis. *Chemical Engineering Research and Design*, *198*, 403–412.
Meakin, P. (1983). Formation of fractal clusters and networks by irreversible diffusion-limited aggregation. *Physical Review Letters*, *51*, 1119–1122.
Meakin, P. (1987). Fractal aggregates. *Advances in Colloid and Interface Science*, *28*, 249–331.
Mebel, A. M., Lin, M. C., Yu, T., & Morokuma, K. (1997). Theoretical study of potential energy surface and thermal rate constants for the $C_6H_5 + H_2$ and $C_6H_6 + H$ reactions. *Journal of Physical Chemistry A*, *101*(17), 3189–3196.
Megaridis Constantine, M., & Dobbins Richard, A. (1989). Comparison of soot growth and oxidation in smoking and non-smoking ethylene diffusion flames. *Combustion Science and Technology*, *66*(1–3), 1–16.
Michelsen, H. A., Colket, M. B., Bengtsson, P. E., D'Anna, A., Desgroux, P., Haynes, B. S., Miller, J. H., Nathan, G. J., Pitsch, H., & Wang, H. (2020). A review of terminology used to describe soot formation and evolution under combustion and pyrolytic conditions. *ACS Nano*, *14*(10), 12470–12490.
Modi, S., Okonkwo, O., Zhou, H., Kavadiya, S., Foston, M. B., & Biswas, P. M. (2023). Geometric model for predicting the size and morphology evolution of multiparticle aggregates during simultaneous reaction and sintering. *Chemical Engineering Journal*, *458*, Article 141423.
Neoh, K. G. (1980). *Soot burnout in flames* (Ph.D. thesis), Boston: Massachusetts Institute of Technology.
Niranjan, R., & Thakur, A. K. (2017). The toxicological mechanisms of environmental soot (black carbon) and carbon black: Focus on Oxidative stress and inflammatory pathways. *Frontiers in Immunology*, *8*(JUN), Article 276079.
Oh, C., & Sorensen, C. M. (1997). Light scattering study of fractal cluster aggregation near the free molecular regime. *Journal of Aerosol Science*, *28*(6), 937–957.
Ono, K., Dewa, K., Matsukawa, Y., Saito, Y., Matsushita, Y., Aoki, H., Era, K., Aoki, T., & Yamaguchi, T. (2017). Experimental evidence for the sintering of primary soot particles. *Journal of Aerosol Science*, *105*, 1–9.
O'Sullivan, D., Diemer, R. B., & Rigopoulos, S. (2025). Derivation of models for the fusing of soot aggregates from carbon black reactor data. *Aerosol Science and Technology*, *59*(4), 451–469.
O'Sullivan, D., & Rigopoulos, S. (2022). A conservative finite volume method for the population balance equation with aggregation, fragmentation, nucleation and growth. *Chemical Engineering Science*, *263*, Article 117925.
Pratsinis, S. E. (1988). Simultaneous nucleation, condensation, and coagulation in aerosol reactors. *Journal of Colloid and Interface Science*, *124*(2), 416–427.
Puri, R., Richardson, T., Santoro, R., & Dobbins, R. (1993). Aerosol dynamic processes of soot aggregates in a laminar ethene diffusion flame. *Combustion and Flame*, *92*(3), 320–333.
Purl, R., Richardson, T. F., Santoro, R. J., & Dobbins, R. A. (1993). Aerosol dynamic processes of soot aggregates in a laminar ethene diffusion flame. *Combustion and Flame*, *92*, 320–333.
Raman, V., & Fox, R. O. (2016). Modeling of fine-particle formation in turbulent flames. *Annual Review of Fluid Mechanics*, *48*, 159–190.
Rigopoulos, S. (2019). Modelling of soot aerosol dynamics in turbulent flow. *Flow, Turbulence and Combustion*, *103*(3), 565–604.
Rigopoulos, S. (2024). *Population balance of particles in flows: From aerosols to crystallisation*. Cambridge University Press.
Saggese, C., Ferrario, S., Camacho, J., Cuoci, A., Frassoldati, A., Ranzi, E., Wang, H., & Faravelli, T. (2015). Kinetic modeling of particle size distribution of soot in a premixed burner-stabilized stagnation ethylene flame. *Combustion and Flame*, *162*(9), 3356–3369.
Santoro, R. J., Semerjian, H. G., & Dobbins, R. A. (1983). Soot particle measurements in diffusion flames. *Combustion and Flame*, *51*, 203–218.
Santoro, R. J., Yeh, T. T., Horvath, J. J., & Semerjian, H. G. (1987). The transport and growth of soot particles in laminar diffusion flames. *Combustion Science and Technology*, *53*(2–3), 89–115.
Schenk, M., Lieb, S., Vieker, H., Beyer, A., Gölzhäuser, A., Wang, H., & Kohse-Höinghaus, K. (2015). Morphology of nascent soot in ethylene flames. *Proceedings of the Combustion Institute*, *35*(2), 1879–1886.

Sewerin, F., & Rigopoulos, S. (2018). An LES-PBE-PDF approach for predicting the soot particle size distribution in turbulent flames. *Combustion and Flame*, *189*, 62–76.

Sorensen, C. M. (2011). The mobility of fractal aggregates: A review. *Aerosol Science and Technology*, *45*(7), 765–779.

Sorensen, C. M., & Roberts, G. C. (1997). The prefactor of fractal aggregates. *Journal of Colloid and Interface Science*, *186*(2), 447–452.

Sun, B., & Rigopoulos, S. (2022). Modelling of soot formation and aggregation in turbulent flows with the LES-PBE-PDF approach and a conservative sectional method. *Combustion and Flame*, *242*, Article 112152.

Sun, B., Rigopoulos, S., & Liu, A. (2021). Modelling of soot coalescence and aggregation with a two-population balance equation model and a conservative finite volume method. *Combustion and Flame*, *229*, Article 111382.

Tang, R., Shang, J., Qiu, X., Gong, J., Xue, T., & Zhu, T. (2024). Origin, structural characteristics, and health effects of atmospheric soot particles: A review. *Current Pollution Reports*, 1–16.

Thajudeen, T., Gopalakrishnan, R., & Hogan, C. J. (2012). The collision rate of nonspherical particles and aggregates for all diffusive knudsen numbers. *Aerosol Science and Technology*, *46*(11), 1174–1186.

Tokmakov, I. V., & Lin, M. C. (2002). Kinetics and mechanism of the OH + $C_6H_6$ reaction: A detailed analysis with first-principles calculations. *Journal of Physical Chemistry A*, *106*(46), 11309–11326.

Tokmakov, I. V., & Lin, M. C. (2004). Combined quantum chemical/RRKM-ME computational study of the Phenyl + Ethylene, Vinyl + Benzene, and H + Styrene reactions. *The Journal of Physical Chemistry A*, *108*(45), 9697–9714.

Tsantilis, S., Kammler, H., & Pratsinis, S. (2002). Population balance modeling of flame synthesis of titania nanoparticles. *Chemical Engineering Science*, *57*(12), 2139–2156, Population balance modelling of particulate systems.

Tsantilis, S., & Pratsinis, S. E. (2000). Evolution of primary and aggregate particle-size distributions by coagulation and sintering. *AIChE Journal*, *46*(2), 407–415.

Veshkini, A., Dworkin, S. B., & Thomson, M. J. (2014). A soot particle surface reactivity model applied to a wide range of laminar ethylene/air flames. *Combustion and Flame*, *161*(12), 3191–3200.

Veshkini, A., Dworkin, S. B., & Thomson, M. J. (2016). Understanding soot particle size evolution in laminar ethylene/air diffusion flames using novel soot coalescence models. *Combustion Theory and Modelling*, *20*(4), 707–734.

Vu, T. V., Zauli-Sajani, S., Poluzzi, V., & Harrison, R. M. (2018). Factors controlling the lung dose of road traffic-generated sub-micrometre aerosols from outdoor to indoor environments. *Air Quality, Atmosphere and Health*, *11*(6), 615–625.

Whitesides, R., Domin, D., Salomón-Ferrer, R., Lester, W. A., & Frenklach, M. (2009). Embedded-ring migration on graphene zigzag edge. *Proceedings of the Combustion Institute*, *32*(1), 577–583.

Whitesides, R., Kollias, A. C., Domin, D., Lester, W. A., & Frenklach, M. (2007). Graphene layer growth: Collision of migrating five-member rings. *Proceedings of the Combustion Institute*, *31*(1), 539–546.

Xiong, Y., Kamal Akhtar, M., & Pratsinis, S. E. (1993). Formation of agglomerate particles by coagulation and sintering—Part II. The evolution of the morphology of aerosol-made titania, silica and silica-doped titania powders. *Journal of Aerosol Science*, *24*(3), 301–313.

Xiong, Y., & Pratsinis, S. E. (1993). Formation of agglomerate particles by coagulation and sintering—Part I. A two-dimensional solution of the population balance equation. *Journal of Aerosol Science*, *24*(3), 283–300.

Zhang, T., & Thomson, M. J. (2016). Development of an improved data analysis approach for combined laser extinction and two-angle elastic light scattering diagnostics of soot aggregates. *Applied Optics*, *55*(4), 920–928.

Zhang, Q., Thomson, M. J., Guo, H., Liu, F., & Smallwood, G. J. (2009). A numerical study of soot aggregate formation in a laminar coflow diffusion flame. *Combustion and Flame*, *156*(3), 697–705.